



Universiteit
Leiden
The Netherlands

Analytical nonadiabatic couplings and gradients within the state-averaged orbital-optimized variational quantum eigensolver

Yalouz, S.; Koridon, E.; Senjean, B.; Lasorne, B.; Buda, F.; Visscher, L.

Citation

Yalouz, S., Koridon, E., Senjean, B., Lasorne, B., Buda, F., & Visscher, L. (2022). Analytical nonadiabatic couplings and gradients within the state-averaged orbital-optimized variational quantum eigensolver. *Journal Of Chemical Theory And Computation*, 18(2), 776-794.
doi:10.1021/acs.jctc.1c00995

Version: Publisher's Version

License: [Licensed under Article 25fa Copyright Act/Law \(Amendment Taverne\)](#)

Downloaded from: <https://hdl.handle.net/1887/3279470>

Note: To cite this publication please use the final published version (if applicable).

Analytical Nonadiabatic Couplings and Gradients within the State-Averaged Orbital-Optimized Variational Quantum Eigensolver

Saad Yalouz,^{*} Emiel Koridon,^{*} Bruno Senjean,^{*} Benjamin Lasorne,^{*} Francesco Buda, and Lucas Visscher



Cite This: *J. Chem. Theory Comput.* 2022, 18, 776–794



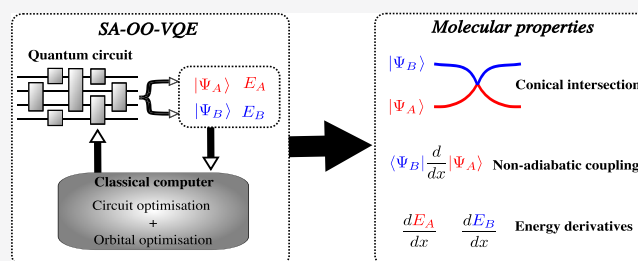
Read Online

ACCESS |

Metrics & More

Article Recommendations

ABSTRACT: We introduce several technical and analytical extensions to our recent state-averaged orbital-optimized variational quantum eigensolver (SA-OO-VQE) algorithm (see Yalouz et al. *Quantum Sci. Technol.* 2021, 6, 024004). Motivated by the limitations of current quantum computers, the first extension consists of an efficient state-resolution procedure to find the SA-OO-VQE eigenstates, and not just the subspace spanned by them, while remaining in the equi-ensemble framework. This approach avoids expensive intermediate resolutions of the eigenstates by postponing this problem to the very end of the full algorithm. The second extension allows for the estimation of analytical gradients and nonadiabatic couplings, which are crucial in many practical situations ranging from the search of conical intersections to the simulation of quantum dynamics, in, for example, photoisomerization reactions. The accuracy of our new implementations is demonstrated on the formaldehyde molecule CH_2NH (a minimal Schiff base model relevant for the study of photoisomerization in larger biomolecules), for which we also perform a geometry optimization to locate a conical intersection between the ground and first-excited electronic states of the molecule.



1. INTRODUCTION

Many fundamental processes in nature, such as photosynthesis and vision, are triggered by light absorption. Thus, a proper description of the associated primary light-induced photochemical events requires a quantum-mechanical approach able to treat accurately both the ground and the excited electronic states. Although density functional theory (DFT) and its time-dependent extension to excited states (TDDFT) have seen huge progress in treating molecular and condensed matter systems near equilibrium,^{2–4} these approaches are not adequate to accurately describe photochemical reaction paths for which the Born–Oppenheimer approximation breaks down for several strongly coupled electronic states that get very close in energy.⁵ Especially couplings between the first excited and ground states are problematic because of the single-reference character of many quantum chemical methods (for instance the popular time-dependent density functional theory, TDDFT approach). While single-reference approaches with spin-flip excitations might help to overcome some of these limitations,⁶ in general more accurate and computationally demanding multiconfigurational wave function approaches are required for modeling these intrinsically nonadiabatic cases. A good example is the description of the prototypical photoisomerization process in the retinal chromophore of rhodopsin, one of the most studied events in photobiology.⁷ Schematically, after the initial photoexcitation, this event proceeds via the

relaxation in the first excited state (S_1) toward a conical intersection (CoIn) region. Here, the population is transferred back to the ground state (S_0) where the isomerization is completed. To describe dynamically this type of event, one needs the knowledge of the potential energy surfaces (PES) for the electronic states involved in the process, typically S_0 and S_1 . Moreover, one should also efficiently compute the gradient of the PES with respect to the nuclear displacement, which in a semiclassical nonadiabatic molecular dynamics scheme provides the forces driving the nuclear subsystem.^{5,7,8} Finally, it is also crucial to estimate the nonadiabatic coupling terms between the two electronic states, which eventually determine the conical topography of the crossing between the two PES and the dynamical coupling that results in population transfer between the two states.^{9,10} The challenge in computational quantum chemistry is to obtain all these necessary ingredients at an affordable numerical cost and yet with good accuracy.

Methods that are able to provide both nonadiabatic couplings and a correct description of the PES topology and

Received: October 4, 2021

Published: January 14, 2022



topography (double cone of dimension two with respect to variations of the nuclear coordinates) of conical intersections require, formally, that the problem be solved at the very end with a final Hamiltonian diagonalization. When the crossing occurs between the first excited and ground states, this implies a democratic treatment of both wave functions within a common Slater determinant basis set, which in practice calls for a state-averaged (SA) orbital optimization. This can be achieved in-principle by the state-averaged multiconfigurational self-consistent field (SA-MCSCF) method.¹¹ In practice, the diagonalization step is the principal bottleneck and one has to consider small complete active spaces (CAS), thus leading to the state-averaged complete active space self-consistent field (SA-CASSCF) method.¹¹ However, this decrease in complexity comes at the expense of a missing dynamical correlation treatment, that is usually recovered by multireference quasidegenerate perturbation techniques, as in the XMS-CASPT2,¹² XMCQDPT2,¹³ or QD-NEVPT2 methods;^{14,15} see also ref 16 for a comparative discussion of the correct treatment of degeneracies with a selection of excited-state approaches.

With the advent of quantum computing, the dream of a very large CAS becomes possible again, thus turning small SA-CASSCF into large SA-CASSCF which should be good enough to account for a qualitatively correct description of the wave function and also include a substantial part of the (previously missing) so-called dynamical correlation. Note that even with relatively small active spaces, the dynamical correlation can be retrieved a posteriori by other techniques on quantum computers, with no additional qubits or circuit depth, but at the expense of more measurements, as described by Takeshita et al.¹⁷ Recently, the *quantum analogue* of SA-CASSCF was introduced by Yalouz et al.¹ based on a state-averaged orbital-optimized (SA-OO) extension of the variational quantum eigensolver (VQE) algorithm,^{18,19} thus referred to as the SA-OO-VQE algorithm. While SA-OO-VQE has been shown to provide an accurate and democratic description of both the ground and first-excited PES,¹ its extension to excited-state quantum dynamics requires the knowledge of energy gradients and nonadiabatic couplings. In this work, we show how these properties can be analytically estimated on a quantum computer within the SA-OO-VQE framework, following the coupled-perturbed equations.^{20–26} In analogy with ref 1, the performance of our algorithm is illustrated on the minimal Schiff base model (i.e., the formaldehyde molecule), for which results are indistinguishable from that of its classical analogue, the (coupled-perturbed) SA-CASSCF method.

The paper is organized as follows. For pedagogical purposes, we briefly introduce quantum chemistry for excited states in section 2.1, from the Born–Oppenheimer approximation in section 2.1.1 to the SA-MCSCF method in section 2.1.2. Turning to quantum computing in section 2.2, a summary of the SA-OO-VQE is given in section 2.2.1, and a way to extract the eigenstates (i.e., the adiabatic states) is provided in section 2.2.2, where we also discuss the alternative choice of having diabatic or adiabatic states within the SA-OO-VQE algorithm. The analytical estimation of energy gradients and nonadiabatic couplings is then described in sections 2.2.3 and 2.2.4, respectively, and they are compared with classical methods in section 4.2. Using the equations for the analytical gradients, a geometry optimization to the degeneracy point is executed in section 4.3 as a simple illustration. A more involved optimization to the minimal energy crossing point (MECI)

that requires the knowledge of nonadiabatic couplings is performed in section 4.4. Conclusions and perspectives are finally discussed in section 5.

2. THEORY

2.1. Quantum Chemistry for Excited States.

2.1.1. Born–Oppenheimer and the Adiabatic Approximation. One of the most fundamental approximations used in theoretical chemistry is the adiabatic approximation between electrons and nuclei, which most often takes the form of the Born–Oppenheimer approximation and sometimes of the Born–Huang approximation (the latter being essentially used for highly accurate treatments of vibrations in small molecules). In both cases, nonadiabatic couplings due to the action of the kinetic energy operator of the nuclei on the parametric dependence of the adiabatic electronic wave functions are neglected; however, the Born–Huang approximation considers nuclear-mass-dependent diagonal corrections that are to be added to the potential energy surface obtained as a single adiabatic eigenvalue of the clamped-nucleus Hamiltonian.

Such approximations are justified by the small ratio of electronic over nuclear masses, which results in very different energy and time scales in the vast majority of cases. However, electronic degeneracies may occur at certain nuclear geometries (Jahn–Teller crossings due to symmetry, or more generally, conical intersections). At such points, the two intersecting potential energy surfaces take locally the shape of a double cone (over a subspace of dimension 2 for a two-state crossing). The two nuclear displacements that lift degeneracy to first order are usually called branching-space vectors; their directions can be identified by the energy gradient difference and first-order nonadiabatic coupling (NAC) vector. Formally, the x -component of the NAC vector between two electronic states $|\Psi_I\rangle$ and $|\Psi_J\rangle$ is defined by

$$D_{IJ} = \left\langle \Psi_I \left| \frac{\partial}{\partial x} \Psi_J \right. \right\rangle \quad (1)$$

where x represents a given nuclear coordinate and the wave functions depend parametrically on it (integration, however, is performed over the electronic Hilbert space only). If the wave functions considered in eq 1 are exact, they yield

$$D_{IJ} = \frac{1}{E_J - E_I} \langle \Psi_I | \frac{\partial \hat{H}}{\partial x} | \Psi_J \rangle \quad (2)$$

in virtue of the off-diagonal Hellmann–Feynman theorem. The magnitude of the NAC vector is ill-defined at a conical intersection, since it diverges as the inverse of the energy difference (see eq 2). The numerator, however, is well-defined and often called the derivative coupling vector; note that the nomenclature is not fixed in the literature. It can be viewed as a transition gradient. The other vector that forms the branching space together with the derivative coupling is the gradient (half) difference,

$$G_{IJ} = \frac{1}{2} \left(\langle \Psi_I | \frac{\partial \hat{H}}{\partial x} | \Psi_J \rangle - \langle \Psi_J | \frac{\partial \hat{H}}{\partial x} | \Psi_I \rangle \right) \quad (3)$$

The vectors G_{IJ} and $(E_J - E_I)D_{IJ}$ —often denoted g and h vectors or x_1 and x_2 vectors in this context—play symmetrical roles: they form the two directions that make the adiabatic energy difference increase to first order from zero at a conical

intersection. They actually are undetermined up to within a mutual rotation, which directly reflects the freedom in defining two specific degenerate eigenstates (see, e.g., ref 27.).

In addition to being essential for the correct capture of the conical topography of crossings, nonadiabatic couplings are required for describing the coupled equations that govern the nuclear components of the molecular wave function. As already pointed out, they become large when the energy gap between electronic states decreases, which is why conical intersections are key for describing radiationless processes whereby the population is transferred among electronic states. In practice, nonadiabatic quantum dynamics is often better described in terms of quasideadronic states that result from a unitary transformation of a relevant subset of coupled adiabatic states. They vary smoothly enough with respect to nuclear coordinates to allow for neglect of kinetic couplings but introduce instead nonzero potential couplings.

Further on this is beyond the scope of the present work and the literature on the subject is vast. We refer for example to ref 28 for a comprehensive review of relevant concepts. Finally, let us stress that the ability of a computational method to describe correctly the topography of a conical intersection is intimately related to the formal possibility of using analytic derivative techniques for evaluating nonadiabatic couplings.¹⁶ This somewhat relies on the fact that the final step of the whole computational procedure should be viewed as a Hamiltonian submatrix diagonalization that provides several eigenstates democratically within the same subspace. The state-averaged multiconfigurational self-consistent-field (SA-MCSCF) method is an evident option in this context, with analytic derivatives applied similarly to diagonal and off-diagonal terms.²²

2.1.2. State-Averaged Multiconfigurational Self-Consistent-Field Method (SA-MCSCF). The electronic structure Hamiltonian reads, in second quantization,

$$\hat{H} = \sum_{pq} h_{pq} \hat{E}_{pq} + \frac{1}{2} \sum_{pqrs} g_{pqrs} \hat{E}_{pqrs} \quad (4)$$

where the one- and two-electron integrals are defined as (in real algebra)

$$h_{pq} = \int d\mathbf{r} \phi_p(\mathbf{r}) \left(-\frac{1}{2} \nabla_{\mathbf{r}}^2 + v_{ne}(\mathbf{r}) \right) \phi_q(\mathbf{r}) \quad (5)$$

and

$$g_{pqrs} = \iint d\mathbf{r}_1 d\mathbf{r}_2 \frac{\phi_p(\mathbf{r}_1) \phi_r(\mathbf{r}_2) \phi_q(\mathbf{r}_1) \phi_s(\mathbf{r}_2)}{|\mathbf{r}_1 - \mathbf{r}_2|} \quad (6)$$

respectively, where $\{\phi_p\}$ are the molecular orbitals defining the (finite) basis set and $v_{ne}(\mathbf{r})$ is the nucleus-electron potential. The one- and two-body spin-free excitation operators are defined such as $\hat{E}_{pq} = \sum_{\sigma} \hat{a}_{p\sigma}^{\dagger} \hat{a}_{q\sigma}$ and $\hat{E}_{pqrs} = \sum_{\sigma, \tau} \hat{a}_{p\sigma}^{\dagger} \hat{a}_{r\tau}^{\dagger} \hat{a}_{s\tau} \hat{a}_{q\sigma}$ where $\hat{a}_{p\sigma}^{\dagger}$ ($\hat{a}_{p\sigma}$) is the creation (annihilation) operator of an electron with spin σ in spatial orbital p . Because of the exponential increase of the configuration space in the number of molecular orbitals, it is of common use to select only a restricted (and, ideally, relevant) part of it in practical calculation, for instance by considering the active space approximation where the orbital space is separated into a set of frozen occupied, active, and virtual orbitals. In such a reduced configuration space, the configuration interaction method is not invariant anymore under orbital rotations^{11,29} and the choice of orbitals will influence the quality of the

result. Hence, one has to consider the reoptimization of the orbitals, thus leading to the MCSCF model which wave function reads:

$$|\Psi(\boldsymbol{\kappa}, \mathbf{c})\rangle = e^{-\hat{\kappa}} \left(\sum_i c_i |\Phi_i\rangle \right) \quad (7)$$

where $\{|\Phi_i\rangle\}$ are Slater determinants or configuration state functions, and $\hat{U}_O(\boldsymbol{\kappa}) = e^{-\hat{\kappa}}$ is the orbital-rotation operator. The latter is defined as follows in the spin-restricted formalism with real algebra:

$$\hat{\kappa} = \sum_{p>q}^{\text{MOs}} \kappa_{pq} (\hat{E}_{pq} - \hat{E}_{qp}) \quad (8)$$

The parameters of the wave function in eq 7 are determined by variationally optimizing the expectation value of the energy:

$$E = \min_{\boldsymbol{\kappa}, \mathbf{c}} \frac{\langle \Psi(\boldsymbol{\kappa}, \mathbf{c}) | \hat{H} | \Psi(\boldsymbol{\kappa}, \mathbf{c}) \rangle}{\langle \Psi(\boldsymbol{\kappa}, \mathbf{c}) | \Psi(\boldsymbol{\kappa}, \mathbf{c}) \rangle} \quad (9)$$

To have a democratic description of ground and excited states, one can simultaneously optimize several MCSCF states that are generated from the same orbital basis. As extensively discussed in ref 11, it is convenient to introduce an exponential unitary parametrization of the configuration space with nonredundant variables,

$$\hat{U}_C(\mathbf{S}) = e^{-\hat{S}} \quad (10)$$

where

$$\hat{S} = \sum_J \sum_{K>J} S_{KJ} (|\Psi_K^{(0)}\rangle \langle \Psi_J^{(0)}| - |\Psi_J^{(0)}\rangle \langle \Psi_K^{(0)}|) \quad (11)$$

and

$$|\Psi_I^{(0)}\rangle = \sum_i c_i^{(0)} |\Phi_i\rangle \quad (12)$$

are initial orthonormal states built from the same set of molecular orbitals. Within the SA-MCSCF model, the wave functions are subject to a double-exponential parametrization

$$|\Psi_I(\boldsymbol{\kappa}, \mathbf{S})\rangle = e^{-\hat{\kappa}} e^{-\hat{S}} |\Psi_I^{(0)}\rangle \quad (13)$$

where, according to the generalization of the Rayleigh–Ritz variational principle for an ensemble of ground and excited states,³⁰ the parameters are variationally optimized by minimizing the state-averaged energy

$$E^{\text{SA-MCSCF}} = \min_{\boldsymbol{\kappa}, \mathbf{S}} \sum_I w_I \langle \Psi_I(\boldsymbol{\kappa}, \mathbf{S}) | \hat{H} | \Psi_I(\boldsymbol{\kappa}, \mathbf{S}) \rangle \quad (14)$$

where $\sum_I w_I = 1$ and the states are automatically orthonormalized as they are generated from unitary transformations of the initial orthonormal states $\{|\Psi_I^{(0)}\rangle\}$. Note that due to the orbital optimization, the converged individual and state-averaged energies may vary with the weights. In practice, the equal weight SA-MCSCF (for which all weights are equal) is usually considered. Finally, the dependence on $\boldsymbol{\kappa}$ in the wave functions can actually be transferred to the electronic integrals in the Hamiltonian; that is, $h_{pq} \rightarrow h_{pq}(\boldsymbol{\kappa})$ and $g_{pqrs} \rightarrow g_{pqrs}(\boldsymbol{\kappa})$, such that eq 14 equivalently reads

$$E^{\text{SA-MCSCF}} = \min_{\boldsymbol{\kappa}, \mathbf{S}} \sum_I w_I \langle \Psi_I(\mathbf{S}) | \hat{H}(\boldsymbol{\kappa}) | \Psi_I(\mathbf{S}) \rangle \quad (15)$$

where $\hat{H}(\boldsymbol{\kappa}) = \hat{U}_0^\dagger(\boldsymbol{\kappa})\hat{H}\hat{U}_0(\boldsymbol{\kappa})$ is the MO-basis transformed Hamiltonian.

While the SA-MCSCF method allows for a democratic description of ground and excited states, it is only variational with respect to the state-averaged energy, so that an individual state is not variational. This makes the calculation of analytical energy gradients of each individual state more complicated, as it requires the introduction of specific Lagrangians and the solution of so-called coupled-perturbed equations, as further discussed in section 2.2.3.

2.2. Estimation of Energies, Analytical Gradients, and Nonadiabatic Coupling on a Quantum Computer.

2.2.1. State-Averaged Orbital-Optimized Variational-Quantum-Eigensolver (SA-OO-VQE). The variational quantum eigensolver (VQE)^{18,19} represents one of the most promising methods to estimate the ground-state energy on near-term quantum computers. As suggested by the name of the algorithm, the VQE relies on the Rayleigh–Ritz variational principle and consists of finding the closest approximation to the ground-state wave function thanks to a given *ansatz* (defined by a parametrized unitary operation $\hat{U}(\boldsymbol{\theta})$). Applying this unitary operation to a chosen initial state (usually very easy to prepare, such as the Hartree–Fock (HF) Slater determinant |HF>) leads to a parametrized trial wave function $|\Psi(\boldsymbol{\theta})\rangle = \hat{U}(\boldsymbol{\theta})|\text{HF}\rangle$, from which the associated energy is estimated by repeated measurements of the quantum circuit. Unfortunately, the extension of the VQE algorithm to the excited state is not trivial, as a variational estimation of the excited-state energies can only be defined under orthogonal constraints. Such constraints have been considered by adding penalization terms to the Hamiltonian, thus leading to the state-specific variational quantum deflation (VQD) algorithm^{31–34} where each state is determined by a separate minimization (or only two minimizations in total if the first one is performed on a state-average ensemble³⁵). Other extensions can treat excited states on the same footing, but still favor the ground state.^{36–39} However, the proper description of conical intersections or avoided crossings requires a democratic description of both the ground and excited states. Such an equal footing treatment can be achieved by performing a single minimization (or resolution) for all states sharing the same *ansatz*, as in multistate-contracted VQE (MC-VQE),^{40,41} fully weighted subspace-search VQE (SS-VQE),⁴² variance-VQE,⁴³ and the quantum filter diagonalization method.^{44,45} Inspired by the SS-VQE method of Nakanishi et al.,⁴² we proposed the (equi-weighted) state-averaged orbital-optimized VQE (SA-OO-VQE), that can be seen as a combination of a state-averaged VQE (SA-VQE) and a state-averaged orbital-optimization (SA-OO) procedure. Let us briefly summarize each step of the SA-OO-VQE, focusing on an equi-ensemble of two-states (the extension to more electronic states is straightforward).

1. Initialization: Initialize the circuits with two orthonormal states $|\Phi_A\rangle$ and $|\Phi_B\rangle$.
2. SA-VQE: Apply a quantum *ansatz* (i.e., a given quantum circuit) to transform both initial states into trial states $|\Psi_A(\boldsymbol{\theta})\rangle = \hat{U}(\boldsymbol{\theta})|\Phi_A\rangle$ and $|\Psi_B(\boldsymbol{\theta})\rangle = \hat{U}(\boldsymbol{\theta})|\Phi_B\rangle$, and find the optimal set of *ansätze* parameters that minimizes the state-averaged energy

$$\boldsymbol{\theta}^* = \arg \min_{\boldsymbol{\theta}} E^{\text{SA-OO-VQE}}(\boldsymbol{\kappa}, \boldsymbol{\theta}) \quad (16)$$

for a fixed orbital basis $\boldsymbol{\kappa}$, where the state-average energy reads

$$E^{\text{SA-OO-VQE}}(\boldsymbol{\kappa}, \boldsymbol{\theta}) = w_A \langle \Psi_A(\boldsymbol{\theta}) | \hat{H}(\boldsymbol{\kappa}) | \Psi_A(\boldsymbol{\theta}) \rangle + w_B \langle \Psi_B(\boldsymbol{\theta}) | \hat{H}(\boldsymbol{\kappa}) | \Psi_B(\boldsymbol{\theta}) \rangle \quad (17)$$

where w_A and w_B are the weights attributed to each state with the normalization condition $w_A + w_B = 1$. Note that this energy is lower-bounded by the ensemble energy of the exact two lowest eigenstates (denoted by $|\Psi_0\rangle$ and $|\Psi_1\rangle$) of $\hat{H}(\boldsymbol{\kappa}^*)$ in the active-space approximation, according to the variational principle.³⁰

3. SA-OO: Rotate the orbital basis to find the optimal set of parameters that minimize the state-averaged energy

$$\boldsymbol{\kappa}^* = \arg \min_{\boldsymbol{\kappa}} E^{\text{SA-OO-VQE}}(\boldsymbol{\kappa}, \boldsymbol{\theta}) \quad (18)$$

(e.g., with Newton–Raphson), for a fixed set of parameters $\boldsymbol{\theta}$.

4. SA-OO-VQE: Repeat steps 2 and 3 until the state-average energy is minimized with respect to both $\boldsymbol{\theta}$ and $\boldsymbol{\kappa}$, i.e. find

$$(\boldsymbol{\kappa}^*, \boldsymbol{\theta}^*) = \arg \min_{\boldsymbol{\kappa}, \boldsymbol{\theta}} E^{\text{SA-OO-VQE}}(\boldsymbol{\kappa}, \boldsymbol{\theta}) \quad (19)$$

As discussed in previous works,^{1,42} the lower bound in eq 17 is uniquely defined if $w_A > w_B$, but is invariant under any rotation between $|\Psi_0\rangle$ and $|\Psi_1\rangle$ in the equi-ensemble case ($w_A = w_B$). Hence, considering the case $w_A = w_B$ does not guarantee that the optimized states $|\Psi_A(\boldsymbol{\theta}^*)\rangle$ and $|\Psi_B(\boldsymbol{\theta}^*)\rangle$ are the closest approximation of the eigenstates $|\Psi_0\rangle$ and $|\Psi_1\rangle$. However, this enforces the definition of a well-defined two-state subspace spanned by either Ψ_A and Ψ_B or Ψ_0 and Ψ_1 , such that the latter are eigenstates. Forcing this correspondence (that we refer to as the *state-resolution*) is a complicated task that can be handled in different ways. We can consider that $w_A > w_B$ is a straightforward solution, but this constraint may complicate the SA-VQE optimization considerably.⁴² Additional tricks can be used in the equi-ensemble case, by considering additional cost-functions to be maximized,⁴² a classical diagonalization,⁴⁰ or another type of cost-functions that use the variance of the states.⁴³ In section 2.2.2, we discuss another approach, inspired by the one of Nakanishi,⁴² to solve the state-resolution of a two-state ensemble within the SA-OO-VQE algorithm, when the initial states are the HF Slater determinant and any singlet singly excited configuration interaction (CIS) state. Note that while we focus on those particular initial states in this manuscript, any other choice could in principle be considered.

2.2.2. State-Resolution Procedure. In this section, we propose another method to capture the active-space eigenvectors of $\hat{H}(\boldsymbol{\kappa})$, which requires a few additional gates and a negligible increase in the number of measurements. Our approach consists of taking advantage of the rotational invariance of the equi-ensemble state-averaged energy, in order to postpone the state-resolution to the very end of the SA-OO-VQE algorithm. Considering the equi-ensemble (i.e., $w_A = w_B$), after convergence of the SA-OO-VQE algorithm, the resulting Hilbert space spanned by $|\Psi_A(\boldsymbol{\theta}^*)\rangle$ and $|\Psi_B(\boldsymbol{\theta}^*)\rangle$ is a good approximation to the subspace spanned by the SA-CASSCF states—classical analogue of the SA-OO-VQE

method, within the same active space. (As discussed in section 2.2.1, the SA-OO-VQE states are not constrained to be the eigenvectors of \hat{H} , or, equivalently, to form the adiabatic basis that diagonalizes $\hat{H}(\kappa^*)$.) To resolve the ground and first excited SA-OO-VQE eigenstates (which should be good approximations to $|\Psi_0^{\text{SA-CASSCF}}\rangle$ and $|\Psi_1^{\text{SA-CASSCF}}\rangle$), we propose to implement a rotation between the initial states $|\Phi_A\rangle$ and $|\Phi_B\rangle$, such that the new rotated initial states become

$$\begin{aligned} |\Phi_0(\varphi)\rangle &= \cos \varphi |\Phi_A\rangle + \sin \varphi |\Phi_B\rangle \\ |\Phi_1(\varphi)\rangle &= -\sin \varphi |\Phi_A\rangle + \cos \varphi |\Phi_B\rangle \end{aligned} \quad (20)$$

where we have the property $|\Phi_1(\varphi)\rangle = |\Phi_0(\varphi + \pi/2)\rangle$. After applying the ansatz with optimized parameters θ^* , these new rotated initial states evolve to

$$\begin{aligned} |\Psi_0(\varphi, \theta^*)\rangle &= \cos \varphi |\Psi_A(\theta^*)\rangle + \sin \varphi |\Psi_B(\theta^*)\rangle \\ |\Psi_1(\varphi, \theta^*)\rangle &= -\sin \varphi |\Psi_A(\theta^*)\rangle + \cos \varphi |\Psi_B(\theta^*)\rangle \end{aligned} \quad (21)$$

which leads to a rotation between the final SA-OO-VQE states. Note that they remain orthonormal and, by virtue of the ensembles properties, lead to the same state-averaged energy that is invariant with respect to φ . The state-resolution amounts to finding the value $\varphi \rightarrow \varphi^*$ that minimizes the energy of $|\Psi_0(\varphi, \theta^*)\rangle$,

$$\varphi^* = \arg \min_{\varphi} \langle \Psi_0(\varphi, \theta^*) | \hat{H}(\kappa^*) | \Psi_0(\varphi, \theta^*) \rangle \quad (22)$$

(or, equivalently, maximizes the one of $|\Psi_1(\varphi, \theta^*)\rangle$), thus making both $|\Psi_0(\varphi, \theta^*)\rangle$ and $|\Psi_1(\varphi, \theta^*)\rangle$ approximated eigenstates of $\hat{H}(\kappa^*)$. Satisfying eq 22 can be seen as the fifth step of the SA-OO-VQE algorithm (see section 2.2.1 for the first four steps). In Figure 1, we show the short-depth circuit we specifically developed to perform the rotation between the HF determinant $|\Phi_A\rangle = |\text{HF}\rangle$ and a singlet-excited CIS state $|\Phi_B\rangle = -\hat{E}_{\text{hl}}|\text{HF}\rangle/\sqrt{2}$, where “h” and “l” refer to the HOMO and LUMO orbitals, respectively. In practice, the circuit works as follows (for the sake of simplicity, we focus on a 2-spatial-orbital (4-spin-orbital), that is, 4-qubit—and 2-electron CAS). Starting with the four qubits in the $|0\rangle$ state, a $R_y(2\varphi)$ rotation gate and a X gate are applied to the first and second qubit, respectively, thus leading to the quantum superposition

$$R_y^0(2\varphi)X^1|0000\rangle = \cos \varphi |0100\rangle + \sin \varphi |1100\rangle \quad (23)$$

Then, a controlled-Hadamard gate transforms the state $|1100\rangle$ into $\frac{1}{\sqrt{2}}(|1100\rangle + |1101\rangle)$, which evolves into $\frac{1}{\sqrt{2}}(|1110\rangle + |0001\rangle)$ after applying three CNOT gates. The first term in the right-hand side of eq 23 remains invariant with respect to the aforementioned operations, such that the state now reads

$$\cos \varphi |0100\rangle + \frac{\sin \varphi}{\sqrt{2}}(|1110\rangle + |0001\rangle) \quad (24)$$

Finally, we apply X and Z gates to the first and last qubits, respectively, to arrive at the final expression

$$\begin{aligned} |\Phi_0(\varphi)\rangle &= \cos \varphi |1100\rangle + \frac{\sin \varphi}{\sqrt{2}}(|0110\rangle - |1001\rangle) \\ &= \cos \varphi |\Phi_A\rangle + \sin \varphi |\Phi_B\rangle \end{aligned} \quad (25)$$

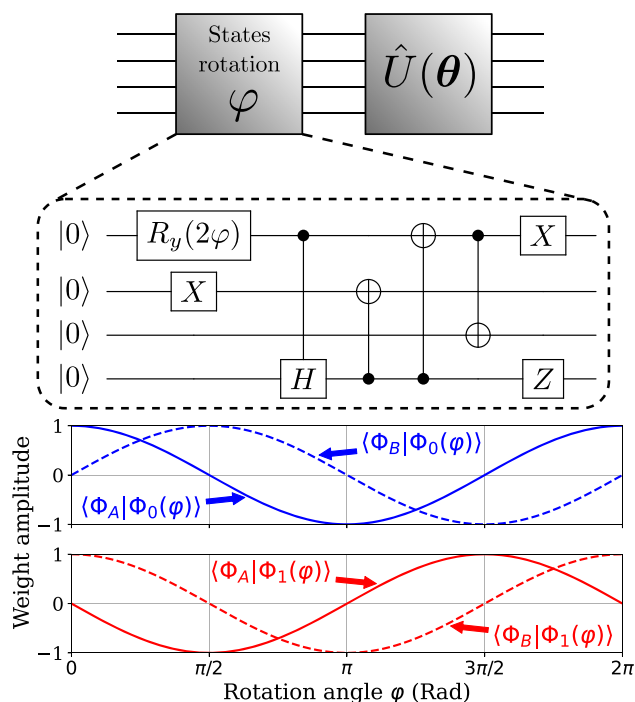


Figure 1. (Top panel) Short-depth quantum circuit specifically designed for the state-resolution of the SA-OO-VQE algorithm, to build the state $|\Phi(\varphi)\rangle = \cos \varphi |\Phi_A\rangle + \sin \varphi |\Phi_B\rangle$, that is, a rotation between the HF state $|\Phi_A\rangle = |\text{HF}\rangle$ and the HOMO–LUMO singlet CIS state $|\Phi_B\rangle = \hat{E}_{\text{hl}}|\text{HF}\rangle/\sqrt{2}$. (Bottom panel) Overlaps $\langle \Phi_A | \Phi_{0/1}(\varphi) \rangle$ and $\langle \Phi_B | \Phi_{0/1}(\varphi) \rangle$ as a function of the rotation parameter φ (with $|\Phi_A\rangle = |\text{HF}\rangle$ and $|\Phi_B\rangle = \hat{E}_{\text{hl}}|\text{HF}\rangle/\sqrt{2}$).

where $|\Phi_A\rangle = |\text{HF}\rangle$ and $|\Phi_B\rangle = -\hat{E}_{\text{hl}}|\text{HF}\rangle/\sqrt{2} = (|0110\rangle - |1001\rangle)/\sqrt{2}$ is the HOMO–LUMO singlet-excited CIS state. Replacing $\varphi \rightarrow \varphi + \pi/2$ in eq 25, one recovers $|\Phi_1(\varphi)\rangle$ in eq 20, such that the parameter φ can be tuned to realize any real linear combination between $|\Phi_A\rangle$ and $|\Phi_B\rangle$, as illustrated in the lower panels of Figure 1. Note that this circuit is valid for any singlet-excited CIS state $|\Phi_B\rangle$, by simply applying the quantum gates to the qubits associated with the orbitals involved in the excitation.

Note that the idea introduced here for the state-resolution procedure in SA-OO-VQE follows closely the one proposed by Nakanishi et al. (Sec II.A. of ref 42). Indeed, the additional operation $V(\varphi)$, for which we provide an explicit form for any two-state ensemble (with a specific focus on initial states that are the HF and any singlet-excited CIS states). Note also that SA-OO and SA-VQE algorithms are alternatively employed in our method. The resulting SA-OO-VQE subspace is then more meaningful in terms of electronic correlations as it (ideally) provides analog results as in the SA-CASSCF method, contrary to the SS-VQE scheme that is equivalent to the CASCI method. Because we work with an equi-ensemble, the state-resolution can be performed at the very end of the SA-OO-VQE algorithm only. This attractive feature of the equi-ensemble SA-OO-VQE allows in principle to spare a lot of unnecessary quantum resources, as one can still end up with the (approximate) eigenstates without requiring harder optimization procedures or additional quantum measurements at each instance of the SA-VQE algorithm.

2.2.3. Analytical Gradients. Molecular properties can be accessed by estimating energy gradients with respect to a given

perturbation.⁴⁶ Analytical expressions, that are less expensive and more precise than finite difference techniques, have been derived in the context of ground-state VQE in refs 47–50. In this section, we turn toward the question of the analytical evaluation of the individual-state nuclear energy gradient with the SA-OO-VQE algorithm (which will be noted $|\Psi_I\rangle$, with $I = 0, 1, \dots$). As opposed to the state-specific orbital-optimized VQE introduced by Mizukami et al.⁵¹ and Takeshita et al.,¹⁷ each set of variational parameters (in our case θ and κ) is not optimized to minimize each individual-state energy,

$$\frac{\partial E_I(\kappa, \theta)}{\partial \kappa_{pq}} \neq 0, \frac{\partial E_I(\kappa, \theta)}{\partial \theta_n} \neq 0 \quad (26)$$

but rather to minimize the state-averaged energy,

$$\frac{\partial E_{SA}(\kappa, \theta)}{\partial \kappa_{pq}} = \frac{\partial E_{SA}(\kappa, \theta)}{\partial \theta_n} = 0 \quad (27)$$

where in both eq 26 and eq 27 it is implicit that the gradients are evaluated at the converged parameters. This renders the estimation of the individual-state nuclear energy gradients more complicated, as it has to take into account the nonvariational character of the method. Fortunately, one can build analytical Lagrangians that are fully variational with respect to every parameter,⁵² such that their optimization facilitates the estimation of the targeted quantities (e.g., energy derivatives and nonadiabatic couplings in our case).

Following this strategy, we build an individual-state Lagrangian \mathcal{L}_I that depends on all the parameters as follows,

$$\mathcal{L}_I = E_I + \left(\sum_{pq} \bar{\kappa}_{pq}^I \frac{\partial E_{SA}}{\partial \kappa_{pq}} - 0 \right) + \left(\sum_n \bar{\theta}_n^I \frac{\partial E_{SA}}{\partial \theta_n} - 0 \right) \quad (28)$$

Note that, on the basis of the state-averaged variational conditions given in eq 27, the correspondence $\mathcal{L}_I = E_I$ holds here. In the definition of the Lagrangian \mathcal{L}_I , the parameters $\bar{\kappa}_{pq}^I$ and $\bar{\theta}_n^I$ are Lagrange multipliers designed to make it fully stationary such that

$$\frac{\partial \mathcal{L}_I}{\partial \bar{\kappa}_{pq}^I} = \frac{\partial \mathcal{L}_I}{\partial \bar{\theta}_n^I} = \frac{\partial \mathcal{L}_I}{\partial \kappa_{pq}} = \frac{\partial \mathcal{L}_I}{\partial \theta_n} = 0 \quad (29)$$

To fulfill the stationary conditions in eq 29, the Lagrange multipliers are determined by solving the so-called coupled-perturbed equations

$$\begin{aligned} \frac{\partial \mathcal{L}_I}{\partial \kappa_{rs}} &= \frac{\partial E_I}{\partial \kappa_{rs}} + \sum_{pq} \bar{\kappa}_{pq}^I H_{pq,rs}^{OO} + \sum_n \bar{\theta}_n^I H_{n,rs}^{CO} = 0 \\ \frac{\partial \mathcal{L}_I}{\partial \theta_m} &= \frac{\partial E_I}{\partial \theta_m} + \sum_{pq} \bar{\kappa}_{pq}^I H_{pq,m}^{OC} + \sum_n \bar{\theta}_n^I H_{n,m}^{CC} = 0 \end{aligned} \quad (30)$$

where we have introduced

$$H_{pq,rs}^{OO} = \frac{\partial^2 E_{SA}}{\partial \kappa_{pq} \partial \kappa_{rs}} \quad (31)$$

$$H_{n,m}^{CC} = \frac{\partial^2 E_{SA}}{\partial \theta_n \partial \theta_m} \quad (32)$$

$$H_{n,rs}^{CO} = \frac{\partial^2 E_{SA}}{\partial \theta_n \partial \kappa_{rs}} \quad (33)$$

which correspond to matrix elements of the (state-averaged) orbital Hessian \mathbf{H}^{OO} , circuit Hessian \mathbf{H}^{CC} and circuit-orbital Hessian \mathbf{H}^{CO} (with $\mathbf{H}^{CO} = (\mathbf{H}^{OC})^T$). The remaining terms

$$G_{rs}^{O,I} = \frac{\partial E_I}{\partial \kappa_{rs}} \quad \text{and} \quad G_m^{C,I} = \frac{\partial E_I}{\partial \theta_m} \quad (34)$$

are elements of the circuit gradient vector $\mathbf{G}^{C,I}$ and the orbital gradient vector $\mathbf{G}^{O,I}$ of the state $|\Psi_I(\theta)\rangle$. The orbital gradient for individual states $G_{pq}^{O,I}$ can be relatively easily computed from their one- and two-RDMs and MO coefficients. The state-averaged orbital Hessian $H_{pq,rs}^{OO}$ can also be determined from the state-averaged one- and two-RDMs and MO coefficients.^{21,25} Therefore, they do not require any additional measurements on the quantum computer. However, the first and second derivatives of the state-averaged energy with respect to the ansätze parameters require many more measurements (but no additional qubits or deeper circuit depth). According to the parameter-shift rule,⁵³ 2^{2n} and 2^{4n} measurements are required to compute the gradient and Hessian with respect to ansätze parameters, respectively, for an ansatz with up to n -fold Fermionic excitation operators. Note that $n = 2$ is usually considered, as the trotterized-UCCSD ansatz can be made arbitrarily exact, as shown by Evangelista et al.,⁵⁴ thus corresponding to 16 and 256 expectation values per element of the \mathbf{H}^{CO} and \mathbf{H}^{CC} matrices, respectively. Finally, the number of parameter-shifted RDMs to be measured on the quantum computer is directly related to the number of ansätze-parameters N_p . For the circuit-orbital Hessian \mathbf{H}^{CO} , N_p parameter-shifted RDMs need to be measured, while $N_p(N_p + 1)/2$ are required to estimate the (symmetric) circuit–circuit Hessian matrix \mathbf{H}^{CC} . The total number of ansätze-parameters also scales with the number of active orbitals as $O(N_{\text{act}}^4)$ for the generalized UCCD ansatz considered in this work. For the sake of conciseness, we refer the interested reader to Appendix A for more details about the estimation of the above Hessian matrices and gradients vectors.

Assuming we have evaluated the necessary Hessian matrices and gradient vectors out of a quantum circuit following Appendix A, the Lagrange multipliers $\bar{\kappa}_{pq}^I$ and $\bar{\theta}_n^I$ satisfying the conditions in eq 29 are determined on a classical computer by solving the following matrix equation

$$\begin{pmatrix} \mathbf{H}^{OO} & \mathbf{H}^{OC} \\ \mathbf{H}^{CO} & \mathbf{H}^{CC} \end{pmatrix} \begin{pmatrix} \bar{\kappa}^I \\ \bar{\theta}^I \end{pmatrix} = - \begin{pmatrix} \mathbf{G}^{O,I} \\ \mathbf{G}^{C,I} \end{pmatrix} \quad (35)$$

Inserting these Lagrange multipliers back into eq 28 makes the Lagrangian fully stationary, and the property $\frac{dE_I}{dx} = \frac{d\mathcal{L}_I}{dx} = \frac{\partial \mathcal{L}_I}{\partial x}$ holds.⁵² Hence, the energy derivative $\frac{dE_I}{dx}$ can be evaluated as follows:

$$\begin{aligned} \frac{dE_I}{dx} &= \sum_{pq} \frac{\partial h_{pq}}{\partial x} \gamma_{pq}^{I,\text{eff}} + \frac{1}{2} \sum_{pqrs} \frac{\partial g_{pqrs}}{\partial x} \Gamma_{pqrs}^{I,\text{eff}} \\ &\quad + \sum_J \sum_n w_J \bar{\theta}_n^I G_n^{C,J} \left(\frac{\partial \hat{H}}{\partial x} \right) \end{aligned} \quad (36)$$

with effective 1- and 2-RDMs defined by

$$\gamma^{I,\text{eff}} = \gamma^I + \tilde{\gamma}^{I,\text{SA}} \quad (37)$$

$$\Gamma^{I,\text{eff}} = \Gamma^I + \tilde{\Gamma}^{I,\text{SA}} \quad (38)$$

where $\gamma_{pq}^I = \langle \Psi_I | \hat{E}_{pq} | \Psi_I \rangle$ and $\Gamma_{pqrs}^I = \langle \Psi_I | \hat{e}_{pqrs} | \Psi_I \rangle$ are regular RDMs of the reference state $|\Psi_I\rangle$, supplemented by corrective state-averaged RDMs $\tilde{\gamma}^{I,\text{SA}}$ and $\tilde{\Gamma}^{I,\text{SA}}$ (encoding orbital contributions) with matrix elements

$$\tilde{\gamma}_{pq}^{I,\text{SA}} = \sum_o (\gamma_{oq}^{\text{SA}} \bar{\kappa}_{op}^I + \gamma_{po}^{\text{SA}} \bar{\kappa}_{oq}^I) \quad (39)$$

$$\tilde{\Gamma}_{pqrs}^{I,\text{SA}} = \sum_o (\Gamma_{oqrs}^{\text{SA}} \bar{\kappa}_{op}^I + \Gamma_{pors}^{\text{SA}} \bar{\kappa}_{oq}^I + \Gamma_{pqos}^{\text{SA}} \bar{\kappa}_{or}^I + \Gamma_{pqro}^{\text{SA}} \bar{\kappa}_{os}^I) \quad (40)$$

Note that building these effective matrices does not require any additional measures from the quantum circuit as the RDMs γ^I and Γ^I are already evaluated during the SA-OO-VQE to estimate the state-averaged energy. The circuit gradient

$G_n^{C,I} \left(\frac{\partial \hat{H}}{\partial x} \right)$ introduced in eq 36 is defined such that

$$G_n^{C,I} \left(\frac{\partial \hat{H}}{\partial x} \right) = \frac{\partial}{\partial \theta_n} \langle \Psi_I | \frac{\partial \hat{H}}{\partial x} | \Psi_I \rangle \quad (41)$$

and can be estimated out of a quantum circuit in the same way as for a generic energy gradient using for example the parameter-shift rule (cf Appendix A). The change being here that the central operator is now the nuclear derivative of the Hamiltonian $\partial \hat{H} / \partial x$ which can be evaluated on a classical computer as shown in Appendix D. Note that, we also refer the interested reader to Appendix D for practical details about nuclear derivatives of electronic integrals (in eq 36) which can be evaluated on a classical computer with common quantum chemistry packages.

Interestingly, compared to its classical analogue SA-CASSCF, note that a unique set of ansätze parameters θ is considered to simultaneously find both ground and first excited states in SA-OO-VQE, instead of the configuration-interaction (CI) coefficients for each state (denoted by \mathbf{c}_0 and \mathbf{c}_1). This results in a greater reduced size of the parameter space,

$$\dim(\theta) \ll \dim(\mathbf{c}_0) + \dim(\mathbf{c}_1) \quad (42)$$

This has important consequences, as the original CP-MCSCF equations sometimes cannot be solved due to memory issues in storing all the matrix elements of \mathbf{H}^{CC} , although some alternative implementations have been proposed to overcome this problem (see ref 25 and references therein). Hence, the classical complexity in solving the coupled-perturbed equations (eq 35) is considerably reduced in SA-OO-VQE compared to SA-CASSCF, at the expense of a lower accuracy (as the SA-VQE solver is not exact in contrast to SA-CASSCF).

2.2.4. Nonadiabatic Couplings. Nonadiabatic couplings have been calculated recently by Tamiya et al.⁵⁵ in the context of SS-VQE without any orbital optimization. In this work, we provide an analytical approach to estimate nonadiabatic couplings within the SA-OO-VQE algorithm, for which the state-averaged orbital-optimization procedure implies a more involved derivation. The definition and Hellmann–Feynman formula for the NAC, D_{IJ} , have been given above—see eq 1 and eq 2—in the ideal case of exact adiabatic eigenstates. It is well-known in the practical context of an MCSCF ansatz that this term actually splits into two contributions: (i) a typically larger CI-contribution, which obeys a Hellmann–Feynman like

formula (except that eigenstates are now CI-coefficient vectors and the Hamiltonian operator is replaced by its finite matrix representation in the CSF basis set); (ii) a typically smaller CSF-contribution, which accounts for molecular orbital gradients (via both their expansion coefficients and the overlaps among the primitive atomic basis functions); see, e.g., ref 22. While the latter CSF contribution is usually straightforward to estimate, the former CI contribution is a more involved term which should take into account the nonvariational character of MCSCF wave functions. Fortunately, coupled-perturbed equations have been derived to treat this aspect based on the same machinery as for gradient calculation.^{20–26} We employed a similar approach to obtain an analytical estimation of NACs with SA-OO-VQE wave functions. For the sake of conciseness, we will present in the following only the essential equations of our developments (we refer the interested reader to Appendix E where we detail each step of the derivation). In practice, one has to solve the following set of coupled linear equations

$$\begin{pmatrix} \mathbf{H}^{\text{OO}} & \mathbf{H}^{\text{OC}} \\ \mathbf{H}^{\text{CO}} & \mathbf{H}^{\text{CC}} \end{pmatrix} \begin{pmatrix} \bar{\kappa}^{IJ} \\ \bar{\theta}^{IJ} \end{pmatrix} = - \begin{pmatrix} \mathbf{G}^{O,IJ} \\ 0 \end{pmatrix} \quad (43)$$

to determine the NAC Lagrange multipliers $\bar{\kappa}^{IJ}$ and $\bar{\theta}^{IJ}$. In eq 43, we retrieve the same Hessian blocks as for the gradient calculation and $G_{pq}^{O,IJ} = \langle \Psi_I | \partial \hat{H} / \partial \kappa_{pq} | \Psi_I \rangle$ represents the interstate orbital coupling gradient, the elements of which can be easily measured out of a quantum computer (using for example methods provided in ref 42). Once the multipliers are determined using a classical computer, the NAC can be evaluated as follows:

$$\begin{aligned} D_{IJ} = & \frac{1}{E_J - E_I} \left(\sum_{pq} \frac{\partial h_{pq}}{\partial x} \gamma_{pq}^{IJ,\text{eff}} + \frac{1}{2} \sum_{pqrs} \frac{\partial g_{pqrs}}{\partial x} \Gamma_{pqrs}^{IJ,\text{eff}} \right. \\ & \left. + \sum_K \sum_n w_K \bar{\theta}_n^{IK} G_n^{C,K} \left(\frac{\partial \hat{H}}{\partial x} \right) \right) \\ & - \frac{1}{2} \sum_{pq} \gamma_{pq}^{IJ} ((\partial_x p|q) - (q|\partial_x p)) \end{aligned} \quad (44)$$

The effective transition 1- and 2-RDMs introduced here are defined by

$$\gamma^{IJ,\text{eff}} = \gamma^{IJ} + \tilde{\gamma}^{IJ,\text{SA}} \quad (45)$$

$$\Gamma^{IJ,\text{eff}} = \Gamma^{IJ} + \tilde{\Gamma}^{IJ,\text{SA}} \quad (46)$$

and $\tilde{\gamma}^{IJ,\text{SA}}$ and $\tilde{\Gamma}^{IJ,\text{SA}}$ are the orbital contributions to the 1- and 2-RDMs, respectively. These state-averaged matrices are defined in a same way as in eq 39 (where we replace $\bar{\kappa}^I$ by $\bar{\kappa}^{IJ}$). In eq 44, the terms in parentheses encode the off-diagonal Hellmann–Feynman contribution complemented by additional corrective terms accounting for the nonvariational character of the wave functions due to orbital and quantum circuit optimization. The contribution outside the parentheses is the so-called “CSF-term” which formally takes into account the variation of the Slater determinants due to nuclear displacement (see ref 20 for more details). The elements $(\partial_x p|q)$ represent the half-derivative of the MOs’ overlap which can be easily calculated analytically with most quantum chemistry packages. Note the presence of transition 1- and 2-RDMs in eq 44 defined as $\gamma_{pq}^{IJ} = \langle \Psi_I | \hat{E}_{pq} | \Psi_I \rangle$ and $\Gamma_{pqrs}^{IJ} = \langle \Psi_I |$

$\hat{e}_{pqrs} |\Psi_j\rangle$). These matrices can be obtained from a quantum circuit using methods to determine transition matrix elements such as the one provided in ref 42.

3. COMPUTATIONAL DETAILS

To test our theoretical developments, we consider the formalimine molecule CH_2NH , a minimal Schiff base model relevant for the study of the photoisomerization in larger biomolecules (such as the RPSB molecule whose *cis* to *trans* isomerization plays a key role in the visual cycle process^{56–58}). An illustration of the geometry of the molecule is shown in Figure 2a.

In analogy with our previous study,¹ we freeze and constrain the N– CH_2 part of the molecule in the same plane. The interatomic distances are $d_{\text{N–C}} = 1.498 \text{ \AA}$, $d_{\text{C–H}} = 1.067 \text{ \AA}$, $d_{\text{N–H}} = 0.987 \text{ \AA}$ and the angle $\text{N–C–H} = 118.36^\circ$. The second H atom is symmetric to the first one with respect to the N–C axis. The two remaining degrees of freedom characterize the out-of-plane bending angle $\alpha \equiv \text{H–N–C}$ and the dihedral angle $\phi \equiv \text{H–N–C–H}$. For practical calculations, the cc-pVDZ basis is used, and an active space of four electrons in three orbitals (4,3) is considered. The orbital optimization is realized over the 43 spatial-orbitals of the system (for SA-OO-VQE and SA-CASSCF). Reference quantum chemistry calculations are realized with OpenMolcas⁵⁹ (e.g., SA-CASSCF simulation and estimation of the associated gradients and NAC) whereas the Psi4⁶⁰ package is used to provide SA-OO-VQE with the initial data about the molecular system.

The noiseless state-vector simulation of the SA-OO-VQE algorithm is realized using the python quantum computing packages OpenFermion⁶¹ and Cirq.⁶² The ansatz we employ in the SA-VQE algorithm is a generalized unitary coupled cluster ansatz with spin-free double-excitation operators (GUCCD) such that

$$\hat{U}(\theta) = e^{\hat{T}(\theta) - \hat{T}^\dagger(\theta)} \quad (47)$$

$$\hat{T}(\theta) = \sum_{t,\nu,w,u}^{\text{active}} \theta_{t\nu w u} \sum_{\sigma,\tau=\uparrow,\downarrow} \hat{a}_{t\sigma}^\dagger \hat{a}_{\nu\tau}^\dagger \hat{a}_{w\tau} \hat{a}_{u\sigma} \quad (48)$$

Our simulation considers ansätze parameters θ initialized to zero and optimized using the “Sequential Least Squares Programming” (SLSQP) method from the python Scipy package. For each call of SA-VQE, the SLSQP method is run with a maximum number of 500 iterations and a precision threshold of 10^{-8} Ha. The threshold for the global convergence of SA-OO-VQE is also set to 10^{-8} Ha. A homemade python code has been developed to implement the state-averaged Newton–Raphson algorithm required for the SA-OO subalgorithm. For an active space of four electrons in three orbitals, we have a circuit depth of 2688 (+6 for the initial rotation circuit), and we optimize 12 parameters. We refer the interested reader to our previous work¹ for more details about the GUCCD ansatz (such as gate complexity).

4. NUMERICAL RESULTS

4.1. Illustration of the Final State Resolution in SA-OO-VQE. As discussed in section 2.2.2, the SA-OO-VQE states obtained after optimizing the κ and θ parameters do not correspond to the eigenstates of $\hat{H}(\kappa)$, and an additional rotation between the initial states is required (also called state resolution). In Figure 2, we illustrate the convergence of each

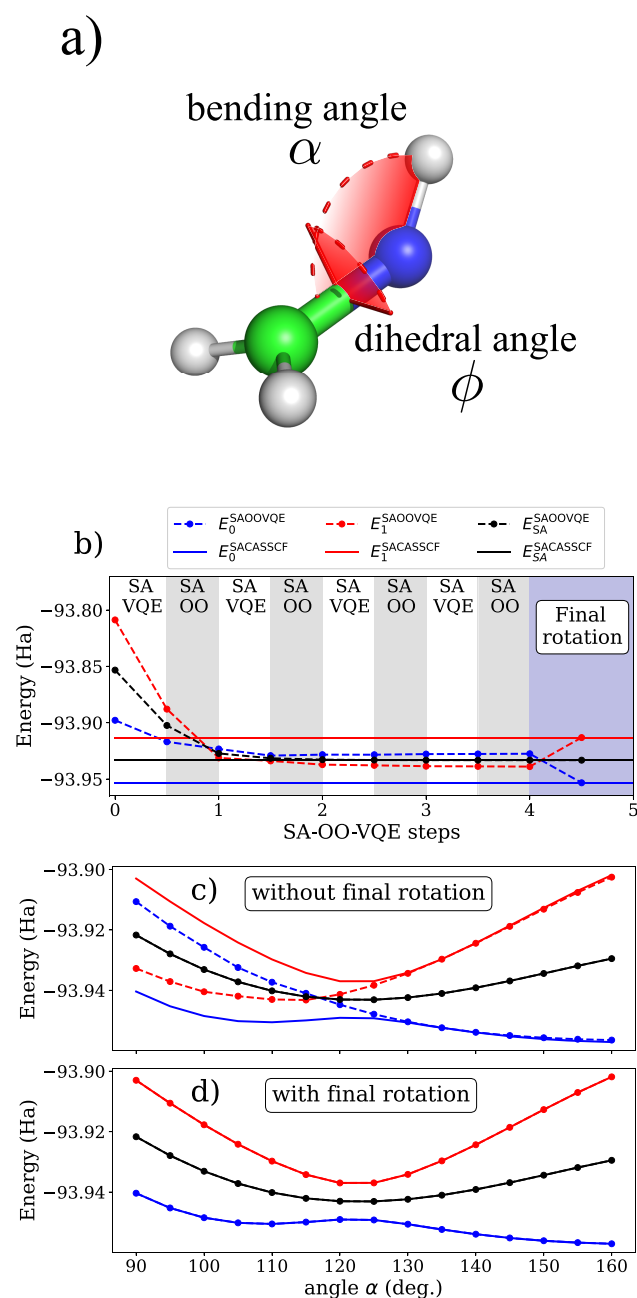


Figure 2. Illustration of the convergence of each step of the equiresonable SA-OO-VQE algorithm. In all panels, dashed and solid lines represent the SA-OO-VQE and SA-CASSCF energies, respectively. (a) Geometry of the formalimine molecule with the bending angle $\alpha = \widehat{\text{NCH}}$ and the dihedral angle $\phi = \widehat{\text{HCNH}}$. (b) Evolution of the state-averaged energy during the different steps of the SA-OO-VQE algorithm for $\phi = 85^\circ$ and $\alpha = 100^\circ$. White and gray strips represent SA-VQE and SA-OO phases, respectively, while the blue strip represents the final state-resolution step. Converged SA-OO-VQE 1D-PES scans along α with $\phi = 85^\circ$ are shown before (c) and after (d) the state-resolution procedure.

step of the SA-OO-VQE algorithm applied to the formalimine molecule, depicted in panel a, with geometry parameters set to $\phi = 80^\circ$ and $\alpha = 100^\circ$. The ground, first-excited and state-averaged energies are plotted on panel b for each step of the SA-OO-VQE algorithm, where SA-VQE and SA-OO phases are represented by white and gray strips,

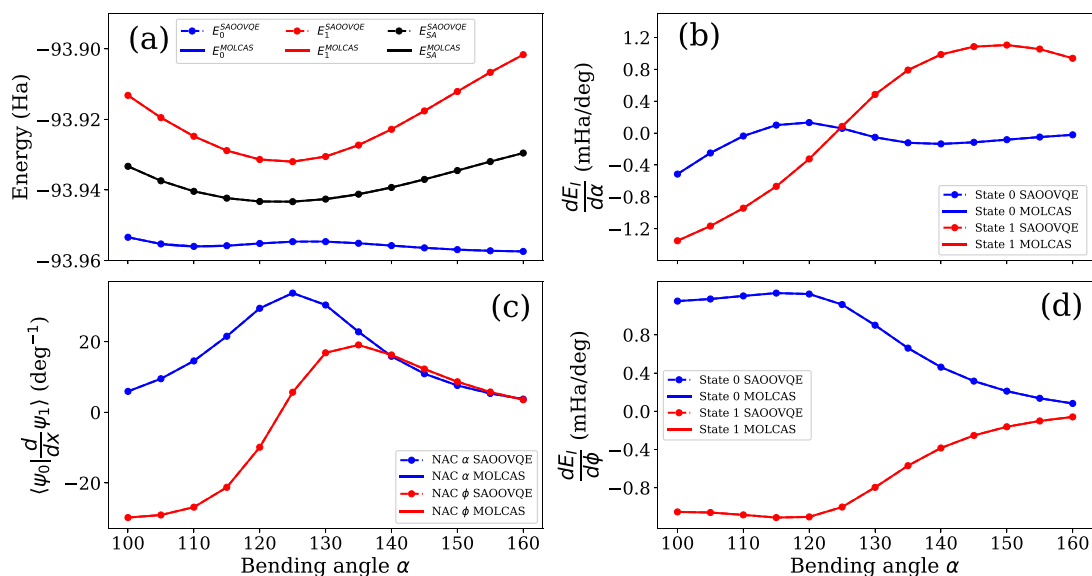


Figure 3. Energy gradients and NAC with respect to the bending angle α with $\phi = 80^\circ$. SA-OO-VQE results are shown in dashed lines with dots while solid lines are for the reference SA-CASSCF results. The ground and first-excited state energies are represented by blue and red colors, respectively: (a) potential energy surfaces; (b) analytical individual-state energy gradients [eq 36 for $x = \alpha$]; (c) nonadiabatic coupling vector $\langle \Psi_0 | (\partial/\partial x) \Psi_1 \rangle$ for $x = \alpha$ (blue) and $x = \phi$ (red); (d) analytical individual-state energy gradients [eq 36 for $x = \phi$].

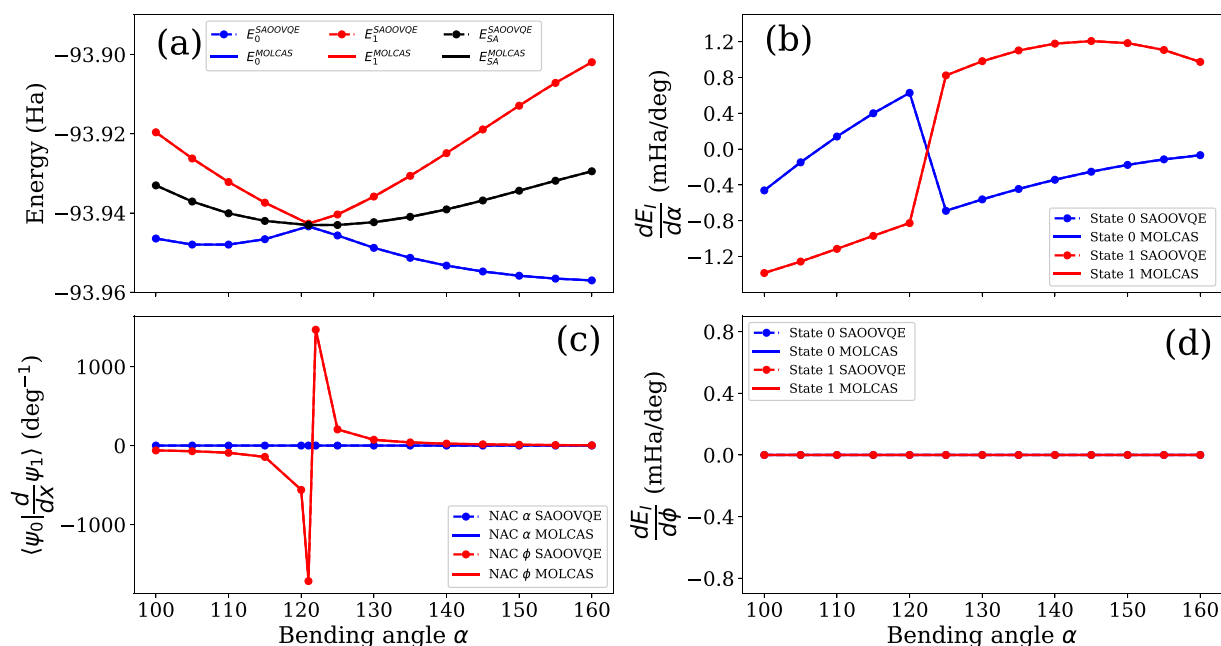


Figure 4. Energy gradients and NAC with respect to the bending angle α with $\phi = 90^\circ$. SA-OO-VQE results are shown in the dashed lines with dots while solid lines are for the reference SA-CASSCF results. The ground and first-excited state energies are represented by blue and red colors, respectively: (a) potential energy surfaces; (b) analytical individual-state energy gradients [eq 36 for $x = \alpha$]; (c) nonadiabatic coupling vector $\langle \Psi_0 | (\partial/\partial x) \Psi_1 \rangle$ for $x = \alpha$ (blue) and $x = \phi$ (red); (d) analytical individual-state energy gradients [eq 36 for $x = \phi$].

respectively. The ground and first-excited SA-CASSCF reference energies are also provided for comparison, as well as the state-averaged SA-CASSCF energy which forms a natural lower bound for SA-OO-VQE (see eq 17). As readily seen in panel b, alternating between the SA-VQE and the SA-OO algorithms progressively lowers the state-averaged energy, requiring three full SA-OO-VQE cycles to reach global convergence. At convergence, this energy has an error of only $\sim 10^{-6}$ Ha with respect to SA-CASSCF, indicating that the subspace spanned by the SA-OO-VQE trial states is a very good approximation to the one spanned by the SA-CASSCF

states. However, the converged individual SA-OO-VQE states differ significantly from the SA-CASSCF states (at the end of the third SA-OO-VQE step in panel b). Hence, one has to apply to state resolution such as described in section 2.2.2 to recover the correct eigenstates. This final step is symbolized by the blue region in panel b, where we employ the rotation circuit shown in Figure 1 and optimize the rotation parameter φ such that the energies are effectively pushed as far as possible from each other, thus maximizing the difference between the first-excited and ground-state energies. After this final step, the individual SA-OO-VQE energies are in very good agreement

with the SA-CASSCF ones (with an error of $\sim 10^{-6}$ Ha, similar to the state-averaged energy error). Note that such agreement is expected, as single and double excitations are enough to span all the electronic configurations in the case of an active space (4,3). Deviations from the SA-CASSCF results may appear when considering larger active spaces.

In panels c and d of Figure 2, we show the one-dimensional (1D) PES along the α -angle for SA-OO-VQE and SA-CASSCF with a dihedral angle $\phi = 85^\circ$. More precisely, we compare the 1D-PES of SA-OO-VQE without (panel c) and with (panel d) the final state-resolution procedure. As readily seen in these two panels, the state-averaged SA-OO-VQE energy is in very good agreement with the reference state-averaged SA-CASSCF energy all over the 1D-PES (with an error $< 10^{-6}$ Ha). Without state resolution (see panel c), the individual-state energies are globally different from the SA-CASSCF ones, especially for $\alpha < 130^\circ$. For $\alpha > 130^\circ$, the energies of the individual states match the reference ones, showing that the state resolution is not always necessary to capture the eigenstates. Interestingly, the SA-OO-VQE states smoothly cross around $\alpha \sim 118^\circ$. As discussed in ref 1, this results from the use of an equi-ensemble where no ordering of the trial states is enforced. In such a case, the converged SA-OO-VQE states will naturally evolve to the state that is the closest to its initial state, that is, with the highest overlap with its initial state (see ref 1 for more details). Typically, when $\alpha < 118^\circ$ the singlet single-excited CIS state $|\Phi_B\rangle = -\hat{E}_{\text{H}}|\text{HF}\rangle$ has the largest contribution to the SA-CASSCF ground state, while for $\alpha > 132^\circ$ the $|\Phi_A\rangle = |\text{HF}\rangle$ has the largest contribution (and reciprocally for the first-excited SA-CASSCF state). The state-resolution procedure (see panel d) will lift the crossing, thus resulting in an avoided-crossing captured by the adiabatic eigenstates and an excellent agreement between the SA-OO-VQE and SA-CASSCF energies.

4.2. Calculation of Analytical Gradients and Non-adiabatic Couplings. Let us now turn to the nuclear gradients and nonadiabatic couplings of the adiabatic states obtained after convergence of the SA-OO-VQE algorithm (with state resolution), following eqs 36 and 44. As mentioned in section 2.2.3, the extra cost for the quantum device is in determining the Hessians \mathbf{H}^{CC} and \mathbf{H}^{OC} . As we have 12 parameters in our simulation, this amounts to 78 and 12 entries of \mathbf{H}^{CC} and \mathbf{H}^{OC} to be computed, respectively. With the parameter shift rule, this becomes a total amount of 19968 and 3072 measurements for \mathbf{H}^{CC} and \mathbf{H}^{OC} , respectively. The rest of the computational work is done on a classical device, given the Hessians and the (transition) 1- and 2-RDM to compute the analytical gradient (nonadiabatic coupling). The results are represented in Figures 3 and 4 along the α direction for $\phi = 80^\circ$ and $\phi = 90^\circ$, respectively. As readily seen in Figures 3 and 4, both the analytical gradients and the NAC calculated from our SA-OO-VQE implementation cannot be distinguished from the SA-CASSCF results, with a negligible difference of the order of 10^{-3} mHa/degree for the gradients and 10^{-3} degree $^{-1}$ for the NAC amplitudes (all over the PES). This supports the derivations of eqs 36 and 44 and shows that SA-OO-VQE can provide (ideally, i.e., without noise) as accurate results as its classical SA-CASSCF analogue. Turning to the energy landscape of Figure 3 (panel a) with $\phi = 80^\circ$ (exactly the same as Figure 2, panel d, but plotted again here for convenience), we observe an avoided crossing between the ground and first-excited states around $\alpha = 125^\circ$. This particular behavior can also be detected by looking at the amplitudes of

the NAC (panel c of Figure 3), which increase significantly at the avoided crossing position (but without diverging).

In contrast, for $\phi = 90^\circ$ (see panel a of Figure 4) the 1D-PES shows a crossing (a conical intersection here). This very different behavior is manifested by a discontinuity in the gradients $\partial E_0/\partial\alpha$ and $\partial E_1/\partial\alpha$ that suddenly invert their position at the crossing point $\alpha \approx 121.5^\circ$, while the gradients are smoothly evolving along the 1D-PES when the states do not cross (see panel b of Figures 3 and 4, respectively). This is a direct consequence of the presence of a degeneracy in the energy profile. In contrast to the α direction (panel b), the fact that the gradients $\partial E_0/\partial\phi$ and $\partial E_1/\partial\phi$ are zero for all α (see panel d in Figure 4) reveals the presence of extrema for both states in the ϕ direction. This behavior is consistent with $\phi = 90^\circ$ defining a mirror-plane symmetry σ_v (C_s point group) wherein there is no interstate coupling (different irreducible representations) and local extrema are induced for both potential energies at $\phi = 90^\circ$. For a better illustration, these local extrema along the ϕ direction are shown in Figure 5 and correspond to the intersection points between the gray plane (defining $\phi = 90^\circ$) and the two-dimensional (α, ϕ)-PESs computed with SA-OO-VQE.

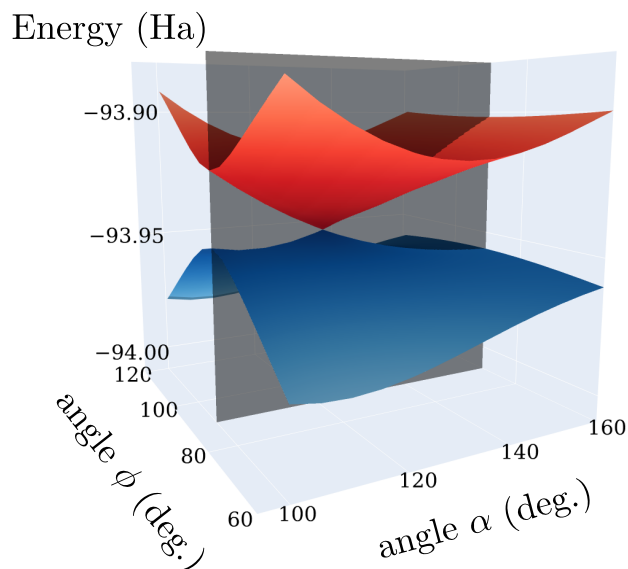


Figure 5. (α, ϕ)-PES for the formaldehyde molecule. The energies are obtained with the SA-OO-VQE algorithm after a full resolution of the states. A conical intersection is observed around the geometry ($\alpha = 121.5^\circ, \phi = 90^\circ$). Gray plane is defined for $\phi = 90^\circ$ and intersects both PESs at extrema values in the ϕ direction.

Considering now the nonadiabatic couplings (panel c of Figure 4), we find that it points to a direction perpendicular to the gradients. This is expected, as the NAC together with the gradient of the energy difference span the branching space defined by α and ϕ , as discussed in section 2.1.1. The NAC exhibits an asymptotic discontinuity around the conical intersection, caused by the term $(E_1 - E_0)^{-1}$ which goes to infinity at this degeneracy point. The increase of the NAC amplitude at the avoided crossing or its divergence at the conical intersection is the expected manifestation of its linear dependence on the inverse of the energy difference (see eq 2). This typically results in a breakdown of the Born–Oppenheimer approximation, which is consistent with

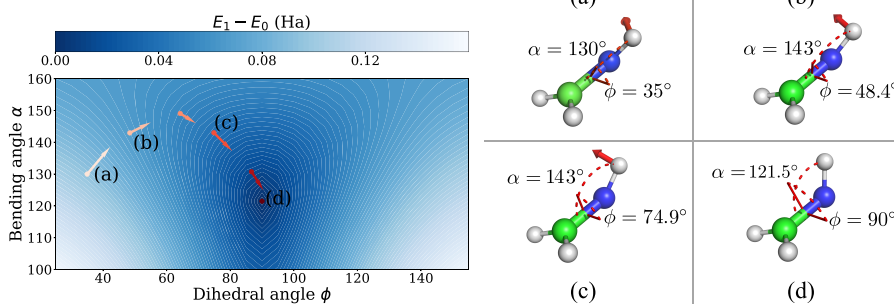


Figure 6. (α, ϕ) -Geometry optimization to the conical intersection point. (Left panel) Optimization path of a steepest-descent algorithm to locate the conical intersection of formaldehyde. The contour plot shows the energy difference $\Delta E = E_1 - E_0$, and the vectors represent the negative of the gradient of the energy difference $\mathbf{g}_{\Delta E}$ at each point of the optimization. (Right panel) Four molecular geometries corresponding to four points of the optimization, denoted by (a), (b), (c) and (d) on the left panel. The corresponding (α, ϕ) angles and $\mathbf{g}_{\Delta E}$ vectors are shown.

observing radiationless population transfer from the first-excited state back to the ground state.

This will essentially occur around such crossing geometries along the photochemical reaction path. A prototypical example is the photoisomerization process in the retinal chromophore of rhodopsin.⁷ In such a situation, quantum dynamics simulations (or their various flavours of quantum-classical approximations) must explicitly account for NAC-terms within the equations of motion for the nuclei evolving within a manifold of coupled electronic states.

4.3. Geometry Optimization to Locate Formaldehyde's Conical Intersection in the (α, ϕ) Space. As an application to the SA-OO-VQE analytical gradients, we perform a geometry optimization inside the (α, ϕ) -plane to find a conical intersection for formaldehyde. To do so, we use a steepest-descent optimization algorithm considering as a cost function the energy difference $\Delta E = E_1^{\text{SAOOVQE}} - E_0^{\text{SAOOVQE}}$. At each step of the run, we update the molecular geometry in the (α, ϕ) -plane based on the associated gradient

$$\mathbf{g}_{\Delta E} = \frac{dE_1^{\text{SAOOVQE}}}{dx} - \frac{dE_0^{\text{SAOOVQE}}}{dx} \quad (49)$$

which is evaluated using our analytical method described in section 2.2 (with $\mathbf{x} = (\alpha, \phi)$).

An example run of the algorithm is shown in Figure 6, in which the steepest-descent procedure starts at point (a) for a molecular configuration $(\alpha, \phi) = (130^\circ, 35^\circ)$. The path followed during the geometry optimization is driven by the vector $-\mathbf{g}_{\Delta E}$ which is illustrated at every four iterations with arrows on the left panel of Figure 6 (out of a total of 20 iterations required to reach a geometry very near the conical intersection point). The last iteration point is also shown, located exactly on the CI. Similarly, on the right panel of Figure 6 the vector $-\mathbf{g}_{\Delta E}$ is represented with red arrows (starting from the hydrogen atom) for four molecular geometries (a), (b), (c), and (d) obtained on the path of optimization (also noted on the left panel). From Figure 6, we see that the path stays orthogonal to isolines ($\Delta E = c$ with c constant) of the cost function ΔE . This feature indicates that the SA-OO-VQE algorithm provides consistent pairs of gradients for the two states, thus leading smoothly to the molecular geometry associated with the conical intersection in the (α, ϕ) -plane. At the end of the geometry optimization, the conical intersection is found for a geometry $\phi = 90^\circ$ and $\alpha = 121.47^\circ$. As a comparison, a similar calculation has been realized with the SA-CASSCF method for which a similar path

was followed in the (α, ϕ) -plane, thus leading to an equivalent location of the conical intersection with a negligible difference of the final molecular geometry ($\sim 0.001^\circ$ error for both α and ϕ). In practice, note that the nonsmooth behavior of the cost function at the conical intersection makes the gradient-descent algorithm hard to converge when approaching this point (as the gradient of the cost function will always have a nonzero component in either direction). As the scope of this paper is to provide proof-of-principle calculation, we simply stopped the algorithm after a limited number of iterations.

4.4. Conical Intersection Optimization in the Full Geometry Space. The previous section focused on the localization of a conical intersection within the (α, ϕ) 2D-subspace at fixed values of the other internal coordinates. As this subspace is a good description of the branching space, there is a unique point of degeneracy (a conical intersection) within this plane where degeneracy is lifted to first order from it. As such, minimizing ΔE , and nothing else, is sufficient, as the complement space is frozen.

In this last section, a step further is realized to characterize the conical intersection of the formaldehyde molecule, by determining the so-called *minimal energy conical intersection* (MECI) of the system. In practice, the MECI point corresponds to the optimal geometry of a given system for which the energies of two states become simultaneously degenerated and maximally lowered. Therefore, it encodes the most favorable molecular conformation for the realization of nonradiative photochemical processes but also intersystem (i.e., spin-forbidden) crossings.^{63,64} As a counterpart, the realization of a geometry optimization to precisely determine the MECI position is usually a pretty involved task. The process implies a full relaxation of the internal coordinates of a molecular system, that is driven by the gradients and NAC vectors of each atom.

Using the estimation of NAC and energy gradients with SA-OO-VQE, we realized a geometry optimization to determine the MECI of formaldehyde, using the so-called gradient projection method.^{65–67} In this algorithm, we simultaneously minimize ΔE^2 —to allow for a smooth minimum—and E_1 , using a steepest-descent algorithm where the minimization follows the direction of a composite gradient. To minimize E_1 only in the direction of the seam space, we project out the component of its gradient along the branching space. The composite gradient is

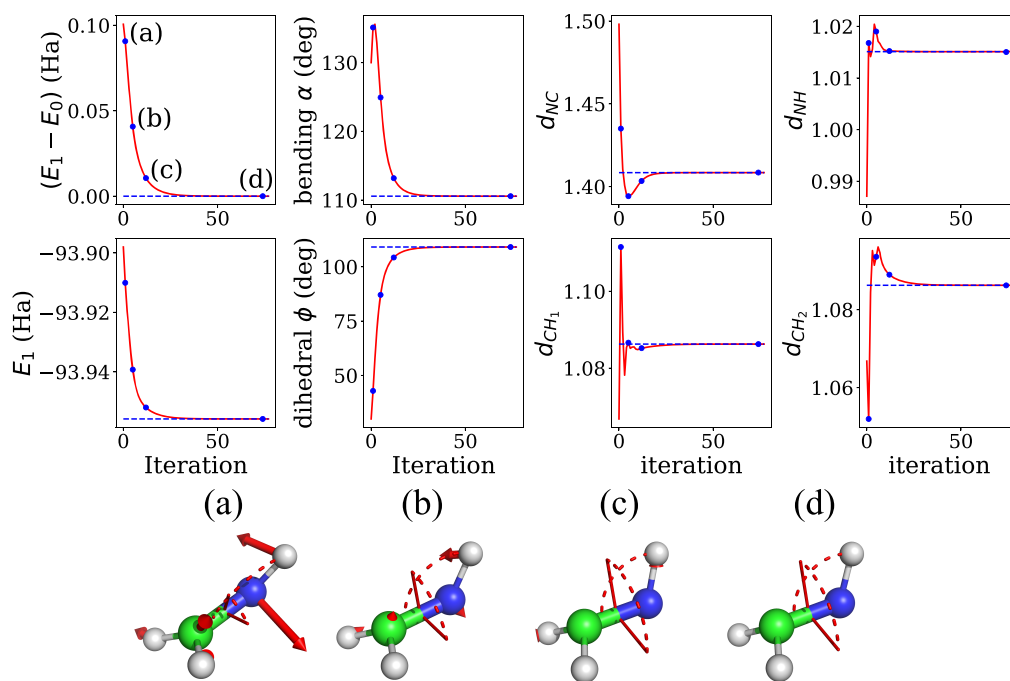


Figure 7. Geometry optimization to minimal energy conical intersection (MECI). (Top panels) Energy difference, first-excited state energy, bending angle, dihedral angle, and bond lengths of the molecule are plotted against the number of iterations to convergence of the MECI optimization using the SA-OO-VQE algorithm (red lines). Dashed blue lines indicate the converged values of the MECI optimization using the SA-CASSCF algorithm. (Bottom panels) Four molecular geometries corresponding to four points of the optimization path (blue points on the top panels). The corresponding gradient vectors $-\mathbf{g}$ are shown for each atom.

$$\mathbf{g} = \eta \left(2\Delta E \frac{\mathbf{g}_{\Delta E}}{|\mathbf{g}_{\Delta E}|} \right) + (1 - \eta) \mathbf{P} \frac{dE_1^{\text{SAOOVQE}}}{dx} \quad (50)$$

where $\eta \in [0, 1]$ is a constant, balancing the two objectives, and

$$\mathbf{P} = 1 - \tilde{\mathbf{g}}_{\Delta E} \tilde{\mathbf{g}}_{\Delta E}^\dagger - \tilde{\mathbf{h}}_{01} \tilde{\mathbf{h}}_{01}^\dagger \quad (51)$$

is the projection along the seam space. Here, \mathbf{h}_{ij} is proportional to the CI-term of the NAC, that is, the first term in eq 44. The tilde indicates the orthonormalization of $\mathbf{g}_{\Delta E}$ and \mathbf{h}_{01} .

Results are laid out in Figure 7. We initialize the algorithm with $\eta = 0.25$ and consider convergence thresholds of 10^{-13} Ha² and 10^{-6} Ha for ΔE^2 and E_1 , respectively. As in the previous section, the starting geometry is $(\alpha, \phi) = (130^\circ, 35^\circ)$, but now all the $3N_{\text{atom}}$ nuclear coordinates move in the direction of their respective gradient defined by eq 50. Our algorithm converges after 78 iterations, where the bending and dihedral angles are $(\alpha, \phi) = (110.6^\circ, 109.1^\circ)$. Note that a dihedral angle of 109.1° here does not break the σ_v mirror symmetry of the molecule, as the hydrogens attached to the carbon bend slightly backward.

As a reference, in Figure 7 dashed lines are used to represent the final results obtained for a similar MECI optimization realized with the SA-CASSCF method (analytical SA-CASSCF gradients and NAC being evaluated with OpenMolcas to drive the optimization). As readily seen in the different plots, the MECI optimization based on SA-OO-VQE (red lines) converges to the same geometry and energies as in SA-CASSCF, thus showing again the accuracy of our estimations of the NAC and energy gradients within the SA-OO-VQE algorithm.

5. CONCLUSIONS AND PERSPECTIVES

In this paper, we introduce several tools to improve our original SA-OO-VQE algorithm.¹ The first improvement consists of introducing a flexible and efficient way to resolve the SA-OO-VQE electronic states. The method, based on ensemble properties, takes advantage of the invariance of the state-averaged energy under rotation of the states involved in the ensemble. Using a simple rotation of the input states (implemented by a short-depth circuit), we show that one can postpone the resolution of the electronic states to the very end of the full SA-OO-VQE scheme, thus avoiding many unnecessary manipulations and quantum measures during intermediate steps of the algorithm. The second improvement is the development of theoretical methods to extract analytical derivatives within the SA-OO-VQE algorithm. These derivatives—the nuclear energy gradients and nonadiabatic couplings—are fundamental for the study of molecular systems, and can be determined using the Lagrangian methods that are intimately linked to the so-called coupled-perturbed theory. The accuracy of our derivations is checked against reference results based on SA-CASSCF calculations, for which we obtain very good agreement. Finally, we illustrate the use of these derivatives in practical calculations by performing the geometry optimization toward the conical intersection of the formal-dimine molecule. The localization of the spectral degeneracy matches perfectly the predictions from the SA-CASSCF method.

The definition of these new tools opens the way to several new developments. One aspect that we already briefly touched upon above, is the definition of the intermediate diabatic and final adiabatic bases. In our implementation of the SA-OO-VQE algorithm, the procedure starts from reference guess states and has no reason to produce “excessive” trans-

formations, thus making the least-transformed subspace a good candidate for being a quasidiabatic representation (see ref 68). At the moment, we have been observing such a property, and we have good incentive but no formal proof. Further work is under way to show that SA-OO-VQE before its final diagonalization (or state-resolution) could indeed be an efficient avenue for the *ab initio* production of relevant quasidiabatic states. Such results would be important as it would facilitate use in molecular quantum dynamics applications. With an appropriate definition of such states and construction of a quantum-classical interface, these tools can benefit from classical implementations⁶⁹ of algorithms to perform various forms of molecular dynamics,^{70,71} thus giving quantum coprocessing a firm place in the toolbox of quantum chemical simulations. A related aspect is to consider different kinds of surface couplings, like those provided by the spin-orbit operator. This is of interest for a range of applications, for example, the rate of intersystem crossing that is key to technological applications, as the construction of more efficient blue light emitting diodes. Here, we note that it is possible to work with a different set of trial states than the Hartree–Fock and the singlet excited model wave functions chosen in the current work. The latter can be replaced by a triplet excited wave function, while the former can also be a nonground state determinant (or other simple wave function) if we are interested in excited-state couplings.

■ CIRCUIT GRADIENT G^C AND HESSIAN H^{CC}

Let us consider the estimation of the expectation value M of a generic operator \hat{M} (in our case the electronic structure Hamiltonian \hat{H}) with respect to a state $|\Psi(\theta)\rangle = \hat{U}(\theta)|\Phi_0\rangle$,

$$M(\theta) = \text{Tr}[\hat{M}\rho(\theta)] = \langle\Psi(\theta)|\hat{M}|\Psi(\theta)\rangle \quad (52)$$

where $\rho(\theta) = |\Psi(\theta)\rangle\langle\Psi(\theta)|$ is the density matrix operator and $\text{Tr}[\cdot]$ is the trace operation. These matrix elements encode the first order (gradient G^C) and second order (Hessian H^{CC}) derivatives with respect to the ansatz parameters θ and read as follows

$$G_i^C = \frac{\partial M(\theta)}{\partial \theta_i} \quad \text{and} \quad H_{ij}^{CC} = \frac{\partial^2 M(\theta)}{\partial \theta_i \partial \theta_j} \quad (53)$$

and can be evaluated with the parameter-shift rule.^{53,73–77}

As a starting point, let us consider the following unitary:

$$U(\theta) = U_1(\theta_1) \times U_2(\theta_2) \\ = (e^{-i\theta_1/2P_1} e^{-i\theta_1/2\tilde{P}_1}) \times (e^{-i\theta_2/2P_2} e^{-i\theta_2/2\tilde{P}_2}) \quad (54)$$

where $[P_1, \tilde{P}_1] = [P_2, \tilde{P}_2] = 0$ with the tilde notation denoting a different Pauli string with the same associated parameters, as this is usually the case in the Fermionic-UCC ansatz. We have $P_j = P_j^\dagger$ and

$$\frac{\partial U_j(\theta_j)}{\partial \theta_j} = -\frac{i}{2}(P_j + \tilde{P}_j)U_j(\theta_j) \quad (55)$$

and

$$\left(\frac{\partial U_j(\theta_j)}{\partial \theta_j}\right)^\dagger = -\frac{\partial U_j(\theta_j)}{\partial \theta_j} \quad (56)$$

We want to estimate the gradient elements

$$G_i^C = \frac{\partial}{\partial \theta_i} \text{Tr}[\hat{M}\rho(\theta)] \quad (57)$$

By taking the derivative with respect to θ_2 , we get

$$G_2^C = \text{Tr}\left[\frac{\partial}{\partial \theta_2} \hat{M}\rho(\theta)\right] \\ = \hat{M}U_1(\theta_1)\left[\frac{\partial U_2(\theta_2)}{\partial \theta_2}\rho U_2^\dagger(\theta_2) + U_2(\theta_2)\rho\left(\frac{\partial U_2(\theta_2)}{\partial \theta_2}\right)^\dagger\right]U_1^\dagger(\theta_1) \\ = -\frac{i}{2}\hat{M}U_1(\theta_1)[(P_2 + \tilde{P}_2)U_2(\theta_2)\rho U_2^\dagger(\theta_2) \\ - U_2(\theta_2)\rho(P_2 + \tilde{P}_2)U_2^\dagger(\theta_2)]U_1^\dagger(\theta_1) \\ = -\frac{i}{2}\hat{M}U_1(\theta_1)U_2(\theta_2)[(P_2 + \tilde{P}_2), \rho]U_2^\dagger(\theta_2)U_1^\dagger(\theta_1) \quad (58)$$

where we used the property $[P_j, U_i(\theta_i)] = 0$ and the notation $\rho = |\Phi_0\rangle\langle\Phi_0|$. We then use the property of commutator for an arbitrary operator [see eq 2 in ref 53, where $U_j(\theta_j) = \exp(-i\theta_j P_j/2)$],

$$[P_j, \rho] = i\left[U_j\left(\frac{\pi}{2}\right)\rho U_j^\dagger\left(\frac{\pi}{2}\right) - U_j\left(-\frac{\pi}{2}\right)\rho U_j^\dagger\left(-\frac{\pi}{2}\right)\right] \quad (59)$$

which can be easily demonstrated by considering the property of exponential of Pauli strings

$$e^{i\theta_j/2P_j} = \cos\left(\frac{\theta_j}{2}\right)\mathbf{1} - i\sin\left(\frac{\theta_j}{2}\right)P_j \quad (60)$$

One then separates $(P_j + \tilde{P}_j)$ as follows:

$$[(P_j + \tilde{P}_j), \rho] = [P_j, \rho] + [\tilde{P}_j, \rho] \quad (61)$$

such that, by inserting eq 59 into eq 58, the gradient reads

$$G_2^C = \frac{1}{2}\hat{M}U_1(\theta_1)(e^{-i/2(\theta_2+\pi/2)P_2} e^{-i/2\theta_2\tilde{P}_2}\rho e^{i/2\theta_2\tilde{P}_2} e^{i/2(\theta_2+\pi/2)P_2} \\ - e^{-i/2(\theta_2-\pi/2)P_2} e^{-i/2\theta_2\tilde{P}_2}\rho e^{i/2\theta_2\tilde{P}_2} e^{i/2(\theta_2-\pi/2)P_2} \\ + e^{-i/2\theta_2P_2} e^{-i/2(\theta_2+\pi/2)\tilde{P}_2}\rho e^{i/2(\theta_2+\pi/2)\tilde{P}_2} e^{i/2\theta_2P_2} \\ - e^{-i/2\theta_2P_2} e^{-i/2(\theta_2-\pi/2)\tilde{P}_2}\rho e^{i/2(\theta_2-\pi/2)\tilde{P}_2} e^{i/2\theta_2P_2})U_1^\dagger(\theta_1) \quad (62)$$

which, by taking the trace of it, leads to the final expression

$$G_2^C = \frac{1}{2}(\langle\hat{M}\rangle_{\theta_2^+} - \langle\hat{M}\rangle_{\theta_2^-} + \langle\hat{M}\rangle_{\tilde{\theta}_2^+} - \langle\hat{M}\rangle_{\tilde{\theta}_2^-}) \quad (63)$$

where the notation $\langle\hat{M}\rangle_{\theta_j^\pm}$ refers to the expectation value of the operator \hat{M} when θ_j has been shifted by $\pm\pi/2$ in front of P_j (and in front of \tilde{P}_j for $\langle\hat{M}\rangle_{\tilde{\theta}_j^\pm}$).

Generalizing eq 63 to any n -fold Fermionic excitation generator \mathcal{G}_j associated with the parameter θ_j leads to the parameter-shift rule:

$$G_j^C = \frac{1}{2} \sum_{n \in \mathcal{G}_j} \langle\langle\hat{M}\rangle_{\theta_n^+} - \langle\hat{M}\rangle_{\theta_n^-}\rangle \quad (64)$$

where θ_n refers to the parameter associated with the Pauli string P_n coming from the Fermionic generator \mathcal{G}_j . Note that the parameter-shift rule only applies to generators \mathcal{G} that have at most two distinct eigenvalues,⁷⁴ which is always the case for any Pauli string but not a linear combination of them. However, each parameter θ_j is associated with two Pauli strings

for a single-excitation Fermionic operator, to eight Pauli strings for a double-excitation Fermionic operator, and to 2^{2n-1} Pauli strings for a n -fold Fermionic excitation operator,^{78,79} such that

$$e^{i\theta/2\mathcal{G}} \rightarrow \prod_{x=1}^{2^{2n-1}} e^{i\theta/2P_x} \quad (65)$$

The above formula is actually an equality because Pauli strings resulting from a same n -fold Fermionic excitation operator actually commute with each other.⁷⁸ Although the Fermionic generator \mathcal{G} usually doesn't have two distinct eigenvalues but three,⁷⁹ they can be decomposed into generators that have only two distinct eigenvalues (for instance, Pauli strings P_x with eigenvalues ± 1) and the gradient can be directly calculated by the product rule and the parameter-shift rule,^{79,80} necessitating 2^{2n} expectation values. So even for a UCCD ansatz, we would need around $2^4 = 16$ expectation values for a single gradient calculation (to be multiplied by the number of parameters).

Turning to the Hessian estimation, one can derive eq 64 with respect to another parameter θ_k ,

$$H_{kj}^{\text{CC}} = \frac{1}{2} \sum_n^{\forall P_n \in \mathcal{G}_j} \left(\frac{\partial}{\partial \theta_k} \langle \hat{M} \rangle_{\theta_n^+} - \frac{\partial}{\partial \theta_k} \langle \hat{M} \rangle_{\theta_n^-} \right) \quad (66)$$

and use the parameter-shift rule again, thus leading to⁷⁵

$$H_{kj}^{\text{CC}} = \frac{1}{4} \sum_n^{\forall P_n \in \mathcal{G}_j} \sum_m^{\forall P_m \in \mathcal{G}_k} (\langle \hat{M} \rangle_{\theta_n^+ \theta_m^+} - \langle \hat{M} \rangle_{\theta_n^+ \theta_m^-} - \langle \hat{M} \rangle_{\theta_n^- \theta_m^+} + \langle \hat{M} \rangle_{\theta_n^- \theta_m^-}) \quad (67)$$

According to eq 67, a single element of the Hessian will require the estimation of 2^{4n} expectation values for a n -fold Fermionic excitation operator.

Different strategies have recently been developed to reduce the number of expectation values required to evaluate an ansatz-parameter gradient of a Fermionic generator \mathcal{G} with more than two distinct eigenvalues. One can consider an additional ancilla qubit and decompose the derivative into a linear combination of unitaries,⁷⁴ or use stochastic strategies^{81,82} or different generator decomposition techniques.^{79,83}

ORBITAL GRADIENT \mathbf{G}^{O} AND HESSIAN \mathbf{H}^{OO}

In this appendix, we show how the orbital gradient and Hessian can be estimated from the one- and two-particle reduced density matrices (1-RDM and 2-RDM) that are measured out of the quantum circuit. For simplicity, let us focus on single wavefunction $|\Psi_I(\boldsymbol{\theta})\rangle$ for which we want to optimize the orbitals. The generalization to a weighted-ensemble of state (as in SA-OO-VQE) is straightforward, as one just has to replace the state-specific 1- and 2-RDMs by the state-averaged 1- and 2-RDMs. The parametrized energy of the state reads

$$E_I(\boldsymbol{\kappa}, \boldsymbol{\theta}) = \langle \Psi_I(\boldsymbol{\theta}) | \hat{U}_O(\boldsymbol{\kappa})^\dagger \hat{\mathcal{H}} \hat{U}_O(\boldsymbol{\kappa}) | \Psi_I(\boldsymbol{\theta}) \rangle \quad (68)$$

where the orbital rotation operator is defined such that

$$\hat{U}_O(\boldsymbol{\kappa}) = e^{-\hat{\kappa}}, \quad \text{with } \hat{\kappa} = \sum_{p>q} \kappa_{pq} \hat{E}_{pq}^- \quad (69)$$

where $\hat{E}_{pq}^- = \hat{E}_{pq} - \hat{E}_{qp}$. Expanding to second order in $\boldsymbol{\kappa}$ the operator $\hat{U}_O(\boldsymbol{\kappa})^\dagger \hat{\mathcal{H}} \hat{U}_O(\boldsymbol{\kappa})$ leads to

$$E_I(\boldsymbol{\kappa}, \boldsymbol{\theta}) \simeq \langle \Psi_I(\boldsymbol{\theta}) | \left(\hat{\mathcal{H}} + [\hat{\kappa}, \hat{\mathcal{H}}] + \frac{1}{2} [\hat{\kappa}, [\hat{\kappa}, \hat{\mathcal{H}}]] \right) | \Psi_I(\boldsymbol{\theta}) \rangle \quad (70)$$

which, when compared to the second-order Taylor expansion of $E_I(\boldsymbol{\kappa})$ with respect to the $\boldsymbol{\kappa}$ parameters,

$$E_I(\boldsymbol{\kappa}, \boldsymbol{\theta}) \simeq E_I(0, \boldsymbol{\theta}) + \boldsymbol{\kappa}^\dagger \mathbf{G}^{\text{O},I} + \frac{1}{2} \boldsymbol{\kappa}^\dagger \mathbf{H}^{\text{OO},I} \boldsymbol{\kappa} \quad (71)$$

allows identification of the MO-gradient and MO-Hessian elements, defined as follows:

$$G_{pq}^{\text{O},I} = \frac{\partial E_I}{\partial \kappa_{pq}} = \langle \Psi_I(\boldsymbol{\theta}) | [\hat{E}_{pq}^-, \hat{\mathcal{H}}] | \Psi_I(\boldsymbol{\theta}) \rangle \quad (72)$$

for the gradient, and

$$H_{pq,rs}^{\text{OO},I} = \frac{\partial^2 E_I}{\partial \kappa_{pq} \partial \kappa_{rs}} = \frac{1}{2} (1 + \mathcal{S}_{(pq)}^{(rs)}) \langle \Psi_I(\boldsymbol{\theta}) | [\hat{E}_{pq}^-, [\hat{E}_{rs}^-, \hat{\mathcal{H}}]] | \Psi_I(\boldsymbol{\theta}) \rangle \quad (73)$$

for the Hessian, where $\mathcal{S}_{(pq)}^{(rs)}$ is an operator that permutes the two couples of indices (pq) and (rs) . In practice, one can derive an analytic form of the orbital gradient and Hessian based on the 1 and 2-RDMs and the electronic integrals. As this derivation is fastidious (and already available in the literature¹¹), we only introduce the final equations required for the implementation. Starting with the orbital gradient $\mathbf{G}^{\text{O},I}$, the elements of the associated matrix read

$$G_{pq}^{\text{O},I} = 2(F_{pq}^I - F_{qp}^I) \quad (74)$$

where the elements of the generalized Fock matrix \mathbf{F}^I (associated with the state $|\Psi_I\rangle$) read

$$F_{pq}^I = \sum_t \gamma_{pt}^I h_{qt} + \sum_{t,u,v} \Gamma_{ptuv}^I g_{qtuv} \quad (75)$$

In practice, building the full matrix can be very expensive. However, and as described in ref 11, considering an active space partitioning does reduce this complexity considerably. In this partitioning, the Fock matrix is fragmented into three contributions:

$$F_{iq}^I = 2(F_{qi}^{\text{frozen},I} + F_{qi}^{\text{active},I}) \quad (76)$$

$$F_{vq}^I = \sum_w^{\text{active}} F_{qw}^{\text{frozen},I} \gamma_{vw}^I + \sum_{w,x,y}^{\text{active}} \Gamma_{vwxy}^I g_{qwxv} \quad (77)$$

and

$$F_{aq}^I = 0 \quad (78)$$

where i , v , and a refer to frozen occupied, active, and virtual MOs, respectively, and $\mathbf{F}^{\text{frozen},I}$ and $\mathbf{F}^{\text{active},I}$ are the so-called frozen and active Fock matrices that read

$$F_{pq}^{\text{frozen},I} = h_{pq} + \sum_i^{\text{frozen}} (2g_{pqii} - g_{piiq}) \quad (79)$$

and

$$F_{pq}^{\text{active},I} = \sum_{w,x}^{\text{active}} \gamma_{wx}^I \left(g_{pqwx} - \frac{1}{2} g_{pxwq} \right) \quad (80)$$

Turning to the orbital Hessian $\mathbf{H}^{\text{OO},I}$, the elements of the associated matrix read

$$H_{pq,rs}^{\text{OO},I} = (1 - S_{pq})(1 - S_{rs}) \left\{ (F_{ps}^I + F_{sp}^I) \delta_{qr} - 2h_{ps} \gamma_{qr}^I + 2 \sum_{t,u} (g_{purv} (\Gamma_{quvs}^I + \Gamma_{quvs}^I) + g_{pruv} \Gamma_{quvs}^I) \right\} \quad (81)$$

where S_{pq} (S_{rs}) is an operator permuting the indices p and q (r and s).

Note that, within the active space approximation, only the 1- and 2-RDM elements from the active space have to be measured on the quantum computer. Every other non-zero terms of the RDMs read

$$\gamma_{ij}^I = \gamma_{ji}^I = 2\delta_{ij} \quad (82)$$

$$\Gamma_{ijkl}^I = 4\delta_{ij}\delta_{kl} - 2\delta_{ij}\delta_{kl} \quad (83)$$

$$\Gamma_{ijwx}^I = \Gamma_{wxij}^I = 2\gamma_{wx}^I \delta_{ij} \quad (84)$$

$$\Gamma_{iwxj}^I = \Gamma_{xjiw}^I = -\gamma_{wx}^I \delta_{ij} \quad (85)$$

where i, j, k, l and w, x denote frozen and active MO indices, respectively.

■ CIRCUIT-ORBITAL HESSIAN \mathbf{H}^{CO}

In practice, one can estimate the off-diagonal blocks of the Hessian matrix \mathbf{H}^{CO} by repeated measurements of the quantum circuit. From the definition of the molecular orbital gradient in eq 72, one obtains

$$\begin{aligned} H_{j,pq}^{\text{CO},I} &= \frac{\partial}{\partial \theta_j} \frac{\partial E_I}{\partial \kappa_{pq}} \\ &= \frac{\partial}{\partial \theta_j} \langle \Psi_I(\theta) | [\hat{E}_{pq}^-, \hat{\mathcal{H}}] | \Psi_I(\theta) \rangle \\ &= \frac{\partial}{\partial \theta_j} \text{Tr}[\hat{M} \hat{\rho}_I(\theta)] \end{aligned} \quad (86)$$

where $\hat{\rho}_I(\theta) = |\Psi_I(\theta)\rangle\langle\Psi_I(\theta)|$ and $\hat{M} = [\hat{E}_{pq}^-, \hat{\mathcal{H}}]$. Using the parameter-shift rule on the operator \hat{M} (see Appendix A), we obtain the elements of $\mathbf{H}^{\text{CO},I}$ as

$$H_{j,pq}^{\text{CO},I} = \frac{1}{2} \sum_n^{\forall p_r \in \mathcal{G}_j} (\langle \hat{M} \rangle_{\theta_n^+} - \langle \hat{M} \rangle_{\theta_n^-}) \quad (87)$$

According to eq 87, one can measure the expectation values of the new operator $\hat{M} = [\hat{E}_{pq}^-, \hat{\mathcal{H}}]$, with the appropriate shift-in-parameter defined from the parameter-shift rule. In practice, eq 87 can be rewritten in terms of generalized Fock matrices,

$$H_{j,pq}^{\text{CO},I} = \sum_n^{\forall p_r \in \mathcal{G}_j} (F_{\theta_n^+,pq}^I - F_{\theta_n^+,qp}^I - F_{\theta_n^-,pq}^I + F_{\theta_n^-,qp}^I) \quad (88)$$

for which elements can be computed according to eq 75, with the 1- and 2-RDMs associated with the θ_n^\pm -shifted state. The elements of the opposite off-diagonal Hessian block are simply built based on the symmetry $\mathbf{H}^{\text{CO}} = (\mathbf{H}^{\text{CO}})^T$.

■ NUCLEAR DERIVATIVE OF THE ELECTRONIC HAMILTONIAN OPERATOR

In the coupled-perturbed equations, one needs the derivative of the Hamiltonian operator with respect to a nuclear coordinate^{21,52,84,85} which is defined by

$$\frac{\partial \hat{\mathcal{H}}}{\partial x} = \sum_{p,q} \frac{\partial h_{pq}}{\partial x} \hat{E}_{pq} + \frac{1}{2} \sum_{p,q,r,s} \frac{\partial g_{pqrs}}{\partial x} \hat{E}_{pqrs} + \frac{\partial E_{\text{nuc}}}{\partial x} \quad (89)$$

where the derivative of the electronic integrals are

$$\frac{\partial h_{pq}}{\partial x} = h_{pq}^{(x)} - \frac{1}{2} \{S^{(x)}, h\}_{pq} \quad (90)$$

$$\frac{\partial g_{pqrs}}{\partial x} = g_{pqrs}^{(x)} - \frac{1}{2} \{S^{(x)}, g\}_{pqrs} \quad (91)$$

where we retrieve “explicit” and “response” terms with respect to a nuclear coordinate. The explicit terms are the ones superscripted with (x) indicating a differentiation of the primitive atomic orbitals (MOs coefficients remaining constant). They are defined such as

$$S_{pq}^{(x)} = \sum_{\mu,\nu}^{\text{AOs}} C_{\mu p} C_{\nu q} \frac{\partial S_{\mu\nu}}{\partial x} \quad (92)$$

$$h_{pq}^{(x)} = \sum_{\mu,\nu}^{\text{AOs}} C_{\mu p} C_{\nu q} \frac{\partial h_{\mu\nu}}{\partial x} \quad (93)$$

$$g_{pqrs}^{(x)} = \sum_{\mu,\nu,\delta,\gamma}^{\text{AOs}} C_{\mu p} C_{\nu q} C_{\delta p} C_{\gamma r} \frac{\partial g_{\mu\nu\delta\gamma}}{\partial x} \quad (94)$$

where \mathbf{C} is the MO coefficient matrix encoding the optimal orbitals that minimize the state-averaged energy. The “response” terms in curly brackets are defined as

$$\{S^{(x)}, h\}_{pq} = \sum_o (S_{po}^{(x)} h_{oq} + S_{qo}^{(x)} h_{po}) \quad (95)$$

$$\{S^{(x)}, g\}_{pqrs} = \sum_o (S_{po}^{(x)} g_{oqrs} + S_{qo}^{(x)} g_{pors}) \quad (96)$$

$$+ S_{ro}^{(x)} g_{pqos} + S_{so}^{(x)} g_{pqro}) \quad (97)$$

The last term present on the right of eq 89 is the nuclear derivative of the nuclear repulsion energy which is pretty straightforward to compute in practice.

■ ANALYTICAL DERIVATION OF NONADIABATIC COUPLINGS FOR SA-OO-VQE

In this section, we introduce the steps to derive the analytical form of eqs 43 and 44 which define the NAC between two states $|\Psi_I\rangle$ and $|\Psi_J\rangle$. Following ref 22 one splits the complete derivative in the NAC into two contributions,

$$D_{IJ} = \langle \Psi_I | \frac{d}{dx} | \Psi_J \rangle = \langle \Psi_I | \frac{\partial}{\partial x} | \Psi_J \rangle + D_{IJ}^{\text{CSF}} \quad (98)$$

The first term represents the so-called CI term, and the second one the CSF term (see ref 23) that does not appear in the exact theory (see eq 1). The CSF term is readily computed as

$$D_{IJ}^{\text{CSF}} = -\frac{1}{2} \sum_{pq} \gamma_{pq}^{IJ} ((\partial_x p|q) - (q|\partial_x p)) \quad (99)$$

The CI term, however, is more involved. To evaluate this term, we will make use of the off-diagonal Hellmann–Feynman theorem:

$$\left\langle \Psi_I \left| \frac{\partial}{\partial x} \Psi_J \right. \right\rangle = \Delta E^{-1} \left\langle \Psi_I \left| \frac{\partial \hat{H}}{\partial x} \right| \Psi_J \right\rangle \quad (100)$$

Equation 100 is valid if two conditions are met. The first one is that the SA-OO-VQE states $|\Psi_I\rangle$ and $|\Psi_J\rangle$ are good approximations of the exact eigenstates of \hat{H} (to some negligible errors, which is verified numerically in our work). Second, the NAC has to be variational with respect to the orbital rotation parameters κ , the ansatz parameters θ , and the final rotation φ implemented for the state resolution. While the SA-OO-VQE states do not satisfy this condition, one can still make the NAC variational with respect to these parameters by introducing the following Lagrangian:

$$L_{IJ} = \bar{S}_{IJ} + \frac{1}{\Delta E} \left(\sum_{p,q} \bar{\kappa}_{pq}^{IJ} \frac{\partial E_{\text{SA}}}{\partial \kappa_{pq}} + \sum_n \bar{\theta}_n^{IJ} \frac{\partial E_{\text{SA}}}{\partial \theta_n} + \bar{\varphi}^{IJ} \frac{\partial \Delta E}{\partial \varphi} \right) \quad (101)$$

where $\bar{S}_{IJ} = \langle \bar{\Psi}_I | \Psi_J \rangle$ is the overlap between the two states, and the leftmost state is kept constant (as denoted by an overbar) because we *only* want to take the derivative of the right state in the NAC. Compared to the gradient Lagrangian [eq 28], note the presence of the convergence condition $\partial \Delta E / \partial \varphi = 0$ encapsulating the effect of the final state resolution (with $\Delta E \equiv E_J - E_I$). In practice, this condition holds as the final rotation consists in minimizing a given state energy (which is equivalent to maximizing the difference between both individual-state energies). This convergence condition was not needed in the analytical gradient Lagrangian in eq 28 as, in contrast to the NAC, the individual-state energies are already variational with respect to φ . The factor $\bar{\Delta E}$ in eq 101 was introduced for convenience (with the overbar meaning that the energy difference is kept constant).

Now, one has to find the Lagrangian multipliers in eq 101 such that the Lagrangian is fully variational with respect to κ , θ , and φ ,

$$\frac{\partial L_{IJ}}{\partial \kappa_{pq}} = \frac{\partial L_{IJ}}{\partial \theta_n} = \frac{\partial L_{IJ}}{\partial \varphi} = 0 \quad (102)$$

From eq 21, we have

$$\frac{\partial \Delta E}{\partial \varphi} = -4\mathcal{H}_{IJ}, \quad \text{and} \quad \frac{\partial \mathcal{H}_{IJ}}{\partial \varphi} = \Delta E \quad (103)$$

where $\mathcal{H}_{IJ} = \langle \Psi_I | \hat{H} | \Psi_J \rangle$ (we assume that \hat{H} is a real operator). We also introduce the two non-zero derivatives of the overlap \bar{S}_{IJ} that read

$$\left\langle \Psi_I \left| \frac{\partial}{\partial \theta_n} \Psi_J \right. \right\rangle \neq 0, \quad \text{and} \quad \left\langle \Psi_I \left| \frac{\partial}{\partial \varphi} \Psi_J \right. \right\rangle = -1 \quad (104)$$

From these simple relations, one obtains the $\bar{\varphi}^{IJ}$ multiplier as

$$\frac{\partial L_{IJ}}{\partial \varphi} = 0 = -1 - 4\bar{\varphi}^{IJ} \rightarrow \bar{\varphi}^{IJ} = -\frac{1}{4} \quad (105)$$

Combining this result with eq 102 and eq 103 provides the other stationary equations for the orbital parameters,

$$\sum_{rs} \bar{\kappa}_{rs}^{IJ} H_{pq,rs}^{\text{OO}} + \sum_n \bar{\theta}_n^{IJ} H_{pq,n}^{\text{OC}} + \langle \Psi_I | \frac{\partial \hat{H}}{\partial \kappa_{pq}} | \Psi_J \rangle = 0 \quad (106)$$

and for the ansatz parameters,

$$\Delta E \langle \Psi_I | \frac{\partial}{\partial \theta_n} \Psi_J \rangle + \sum_{pq} \bar{\kappa}_{pq}^{IJ} H_{n,pq}^{\text{CO}} + \sum_m \bar{\theta}_m^{IJ} H_{n,m}^{\text{CC}} + \frac{\partial \mathcal{H}_{IJ}}{\partial \theta_n} = 0 \quad (107)$$

where we multiplied both sides by ΔE . Let us define the orbital and circuit gradients, respectively, as follows:

$$G_{pq}^{\text{O},IJ} := \left\langle \Psi_I \left| \frac{\partial \hat{H}}{\partial \kappa_{pq}} \right| \Psi_J \right\rangle \quad (108)$$

$$G_n^{\text{C},IJ} := \Delta E \left\langle \Psi_I \left| \frac{\partial}{\partial \theta_n} \Psi_J \right. \right\rangle + \frac{\partial \mathcal{H}_{IJ}}{\partial \theta_n} = 0 \quad (109)$$

Note that the circuit gradient can actually be set to 0. Indeed, we have

$$\begin{aligned} \frac{\partial \mathcal{H}_{IJ}}{\partial \theta_n} &= \left\langle \frac{\partial}{\partial \theta_n} \Psi_I \left| \hat{H} \right| \Psi_J \right\rangle + 0 + \left\langle \Psi_I \left| \hat{H} \right| \frac{\partial}{\partial \theta_n} \Psi_J \right\rangle \\ &= -\Delta E \left\langle \Psi_I \left| \frac{\partial}{\partial \theta_n} \Psi_J \right. \right\rangle \end{aligned} \quad (110)$$

such that the coupled-perturbed equations read

$$\begin{pmatrix} \mathbf{H}^{\text{OO}} & \mathbf{H}^{\text{OC}} \\ \mathbf{H}^{\text{CO}} & \mathbf{H}^{\text{CC}} \end{pmatrix} \begin{pmatrix} \bar{\kappa} \\ \bar{\theta} \end{pmatrix} = - \begin{pmatrix} \mathbf{G}^{\text{O},IJ} \\ 0 \end{pmatrix} \quad (111)$$

The final form of the CI term of the NAC can now be written as follows,

$$\begin{aligned} D_{IJ}^{\text{CI}} = \frac{\partial L_{IJ}}{\partial x} &= (\Delta E)^{-1} \left(\langle \Psi_I | \frac{\partial \hat{H}}{\partial x} | \Psi_J \rangle + \sum_{p,q} \bar{\kappa}_{pq}^{IJ} \frac{\partial^2 E_{\text{SA}}}{\partial \kappa_{pq} \partial x} \right. \\ &\quad \left. + \sum_n \bar{\theta}_n^{IJ} \frac{\partial^2 E_{\text{SA}}}{\partial \theta_n \partial x} \right) \end{aligned} \quad (112)$$

where the last term has been set to zero, similarly as in eq 110:

$$\begin{aligned} \bar{\varphi} \frac{\partial^2 \Delta E}{\partial \varphi \partial x} &= \frac{\partial}{\partial x} \langle \Psi_I | \hat{H} | \Psi_J \rangle \\ &= -\Delta E \left\langle \Psi_I \left| \frac{\partial \Psi_J}{\partial x} \right. \right\rangle + \Delta E \left\langle \Psi_I \left| \frac{\partial \Psi_J}{\partial x} \right. \right\rangle = 0 \end{aligned} \quad (113)$$

Similar to the analytical gradient calculation, we end up with

$$\begin{aligned}
 D_{IJ} = & \frac{1}{E_j - E_I} \left(\sum_{pq} \frac{\partial h_{pq}}{\partial x} \gamma_{pq}^{IJ, \text{eff}} + \frac{1}{2} \sum_{pqrs} \frac{\partial g_{pqrs}}{\partial x} \Gamma_{pqrs}^{IJ, \text{eff}} \right. \\
 & + \sum_K \sum_n w_K \bar{\theta}_n^{IJ} G_n^{C,K} \left(\frac{\partial \hat{H}}{\partial x} \right) \\
 & \left. - \frac{1}{2} \sum_{pq} \gamma_{pq}^{IJ} ((\partial_x p|q) - (q|\partial_x p)) \right) \quad (114)
 \end{aligned}$$

where the effective transition 1- and 2-RDMs read

$$\gamma^{IJ, \text{eff}} = \gamma^{IJ} + \tilde{\gamma}^{IJ, \text{SA}} \quad (115)$$

$$\Gamma^{IJ, \text{eff}} = \Gamma^{IJ} + \tilde{\Gamma}^{IJ, \text{SA}} \quad (116)$$

where $\gamma_{pq}^{IJ} = \langle \Psi_I | \hat{E}_{pq} | \Psi_J \rangle$ and $\Gamma_{pqrs}^{IJ} = \langle \Psi_I | \hat{e}_{pqrs} | \Psi_J \rangle$ are the transition 1- and 2-RDMs, and

$$\tilde{\gamma}_{pq}^{IJ, \text{SA}} = \sum_o (\gamma_{oq}^{\text{SA} \leftarrow IJ} + \gamma_{po}^{\text{SA} \rightarrow IJ}) \quad (117)$$

$$\tilde{\Gamma}_{pqrs}^{IJ, \text{SA}} = \sum_o (\Gamma_{oqrs}^{\text{SA} \leftarrow IJ} + \Gamma_{pors}^{\text{SA} \leftarrow IJ} + \Gamma_{pqos}^{\text{SA} \leftarrow IJ} + \Gamma_{pqro}^{\text{SA} \leftarrow IJ}) \quad (118)$$

are the state-averaged 1- and 2-RDMs (encoding orbital contributions).

AUTHOR INFORMATION

Corresponding Authors

Saad Yalouz – *Laboratoire de Chimie Quantique, Institut de Chimie, CNRS/Université de Strasbourg, Strasbourg 67000, France*; orcid.org/0000-0002-8818-3379; Email: yalouzaad@gmail.com

Emiel Koridon – *Theoretical Chemistry, Vrije Universiteit, Amsterdam NL-1081 HV, The Netherlands; Instituut-Lorentz, Universiteit Leiden, Leiden 2300 RA, The Netherlands*; Email: emiellkoridon@hotmail.com

Bruno Senjean – *CGM, Univ Montpellier, CNRS, ENSCM, Montpellier 34070, France*; Email: bruno.senjejan@umontpellier.fr

Benjamin Lasorne – *CGM, Univ Montpellier, CNRS, ENSCM, Montpellier 34070, France*; orcid.org/0000-0002-9943-1905; Email: benjamin.lasorne@umontpellier.fr

Authors

Francesco Buda – *Leiden Institute of Chemistry, Leiden University, Leiden 2300 RA, The Netherlands*; orcid.org/0000-0002-7157-7654

Lucas Visscher – *Theoretical Chemistry, Vrije Universiteit, Amsterdam NL-1081 HV, The Netherlands*; orcid.org/0000-0002-7748-6243

Complete contact information is available at: <https://pubs.acs.org/10.1021/acs.jctc.1c00995>

Notes

The authors declare no competing financial interest. As we were finalizing the writing process of this manuscript, a similar work appeared on the arXiv.⁷² While they show how to estimate analytical gradients in several excited-state extensions of VQE (which we only do for SA-OO-VQE), our work adds several features to theirs, such as the analytical estimation of nonadiabatic couplings and a discussion on the capture of

diabatic versus nonadiabatic states within SA-OO-VQE. This paper and ref 72 are therefore complementary, and they both pave the way toward excited-state quantum dynamics with excited-state VQE extensions.

ACKNOWLEDGMENTS

S.Y. acknowledges support from The Netherlands Organization for Scientific Research (NWO/OCW), and the Interdisciplinary Thematic Institute ITI-CSC via the IdEx Unistra (ANR-10-IDEX-0002) within the program Investissement d'Avenir. E.K. acknowledges support from Shell Global Solutions BV.

REFERENCES

- Yalouz, S.; Senjean, B.; Günther, J.; Buda, F.; O'Brien, T. E.; Visscher, L. A state-averaged orbital-optimized hybrid quantum-classical algorithm for a democratic description of ground and excited states. *Quantum Sci. Technol.* **2021**, *6*, 024004.
- Verma, P.; Truhlar, D. G. Status and challenges of density functional theory. *Trends Chem.* **2020**, *2*, 302–318.
- Adamo, C.; Jacquemin, D. The calculations of excited-state properties with Time-Dependent Density Functional Theory. *Chem. Soc. Rev.* **2013**, *42*, 845–856.
- Wang, Z.; Wu, C.; Liu, W. NAC-TDDFT: Time-Dependent Density Functional Theory for Nonadiabatic Couplings. *Acc. Chem. Res.* **2021**, *54*, 3288–3297. PMID: 34448566.
- Rozzi, C. A.; Troiani, F.; Tavernelli, I. Quantum modeling of ultrafast photoinduced charge separation. *J. Condens. Matter Phys.* **2018**, *30*, 013002.
- Minezawa, N.; Nakajima, T. Trajectory surface hopping molecular dynamics simulation by spin-flip time-dependent density functional theory. *J. Chem. Phys.* **2019**, *150*, 204120.
- Gozem, S.; Luk, H. L.; Schapiro, I.; Olivucci, M. Theory and simulation of the ultrafast double-bond isomerization of biological chromophores. *Chem. Rev.* **2017**, *117*, 13502–13565.
- Agostini, F.; Min, S. K.; Abedi, A.; Gross, E. K. U. Quantum-classical nonadiabatic dynamics: Coupled-vs independent-trajectory methods. *J. Chem. Theory Comput.* **2016**, *12*, 2127–2143.
- Faraji, S.; Matsika, S.; Krylov, A. I. Calculations of non-adiabatic couplings within equation-of-motion coupled-cluster framework: Theory, implementation, and validation against multi-reference methods. *J. Chem. Phys.* **2018**, *148*, 044103.
- Lee, S.; Horbatenko, Y.; Filatov, M.; Choi, C. H. Fast and Accurate Computation of Nonadiabatic Coupling Matrix Elements Using the Truncated Leibniz Formula and Mixed-Reference Spin-Flip Time-Dependent Density Functional Theory. *J. Phys. Chem. Lett.* **2021**, *12*, 4722–4728.
- Helgaker, T.; Jorgensen, P.; Olsen, J. *Molecular electronic structure theory*; John Wiley & Sons, 2014.
- Shiozaki, T.; Györfy, W.; Celani, P.; Werner, H.-J. Communication: Extended multi-state complete active space second-order perturbation theory: Energy and nuclear gradients. *J. Chem. Phys.* **2011**, *135*, 081106.
- Granovsky, A. A. Extended multi-configuration quasi-degenerate perturbation theory: The new approach to multi-state multi-reference perturbation theory. *J. Chem. Phys.* **2011**, *134*, 214113.
- Park, J. W. Analytical gradient theory for quasidegenerate N-electron valence state perturbation theory (QD-NEVPT2). *J. Chem. Theory Comput.* **2020**, *16*, 326–339.
- Angeli, C.; Borini, S.; Cestari, M.; Cimiraaglia, R. A quasidegenerate formulation of the second order n-electron valence state perturbation theory approach. *J. Chem. Phys.* **2004**, *121*, 4043–4049.
- Gozem, S.; Melaccio, F.; Valentini, A.; Filatov, M.; Huix-Rotllant, M.; Ferré, N.; Frutos, L. M.; Angeli, C.; Krylov, A. I.; Granovsky, A. A.; et al. Shape of multireference, equation-of-motion coupled-cluster, and density functional theory potential energy

surfaces at a conical intersection. *J. Chem. Theory Comput.* **2014**, *10*, 3074–3084.

(17) Takeshita, T.; Rubin, N. C.; Jiang, Z.; Lee, E.; Babbush, R.; McClean, J. R. Increasing the Representation Accuracy of Quantum Simulations of Chemistry without Extra Quantum Resources. *Phys. Rev. X* **2020**, *10*, No. 011004, DOI: 10.1103/PhysRevX.10.011004.

(18) Peruzzo, A.; McClean, J.; Shadbolt, P.; Yung, M.-H.; Zhou, X.-Q.; Love, P. J.; Aspuru-Guzik, A.; O'Brien, J. L. A variational eigenvalue solver on a photonic quantum processor. *Nature Comm.* **2014**, *5*, 4213.

(19) McClean, J. R.; Romero, J.; Babbush, R.; Aspuru-Guzik, A. The theory of variational hybrid quantum-classical algorithms. *New J. Phys.* **2016**, *18*, 023023.

(20) Lengsfeld, B. H., III; Saxe, P.; Yarkony, D. R. On the evaluation of nonadiabatic coupling matrix elements using SA-MCSCF/CI wave functions and analytic gradient methods. I. *J. Chem. Phys.* **1984**, *81*, 4549–4553.

(21) Stålring, J.; Bernhardsson, A.; Lindh, R. Analytical gradients of a state average MCSCF state and a state average diagnostic. *Mol. Phys.* **2001**, *99*, 103–114.

(22) Lengsfeld, B. H.; Yarkony, D. R. Nonadiabatic interactions between potential energy surfaces: Theory and applications. *Adv. Chem. Phys.* **2007**, *82*, 1–71.

(23) Yarkony, D. *Modern electronic structure theory*; World Scientific, 1995; Vol. 2.

(24) Snyder, J. W., Jr; Hohenstein, E. G.; Luehr, N.; Martínez, T. J. An atomic orbital-based formulation of analytical gradients and nonadiabatic coupling vector elements for the state-averaged complete active space self-consistent field method on graphical processing units. *J. Chem. Phys.* **2015**, *143*, 154107.

(25) Snyder, J. W., Jr; Fales, B. S.; Hohenstein, E. G.; Levine, B. G.; Martínez, T. J. A direct-compatible formulation of the coupled perturbed complete active space self-consistent field equations on graphical processing units. *J. Chem. Phys.* **2017**, *146*, 174113.

(26) Fdez. Galván, I.; Delcey, M. G.; Pedersen, T. B.; Aquilante, F.; Lindh, R. Analytical state-average complete-active-space self-consistent field nonadiabatic coupling vectors: Implementation with density-fitted two-electron integrals and application to conical intersections. *J. Chem. Theory Comput.* **2016**, *12*, 3636–3653.

(27) Gatti, F.; Lasorne, B.; Meyer, H.-D.; Nauts, A. *Applications of Quantum Dynamics in Chemistry*; Springer, 2017; pp 81–109.

(28) Baer, M. *Beyond Born-Oppenheimer: Conical intersections and Electronic nonadiabatic coupling terms*; Wiley Online Library, 2006.

(29) Siegbahn, P. E.; Almlöf, J.; Heiberg, A.; Roos, B. O. The complete active space SCF (CASSCF) method in a Newton–Raphson formulation with application to the HNO molecule. *J. Chem. Phys.* **1981**, *74*, 2384–2396.

(30) Gross, E. K.; Oliveira, L. N.; Kohn, W. Rayleigh-Ritz variational principle for ensembles of fractionally occupied states. *Phys. Rev. A* **1988**, *37*, 2805.

(31) Higgott, O.; Wang, D.; Brierley, S. Variational quantum computation of excited states. *Quantum* **2019**, *3*, 156.

(32) Jones, T.; Endo, S.; McArdle, S.; Yuan, X.; Benjamin, S. C. Variational quantum algorithms for discovering Hamiltonian spectra. *Phys. Rev. A* **2019**, *99*, 062304.

(33) Jouzdani, P.; Bringuier, S.; Kostuk, M. A Method of Determining Excited-States for Quantum Computation. *arXiv(Quantum Physics)*, August 12, 2019, 1908.05238, ver. 1. <https://arxiv.org/abs/1908.05238> (accessed September 8, 2021).

(34) Ibe, Y.; Nakagawa, Y. O.; Yamamoto, T.; Mitarai, K.; Gao, Q.; Kobayashi, T. Calculating transition amplitudes by variational quantum eigensolvers. *arXiv(Quantum Physics)*, February 26, 2020, 2002.11724, ver. 1. <https://arxiv.org/abs/2002.11724> (accessed September 8, 2021).

(35) Wen, J.; Lv, D.; Yung, M.-H.; Long, G.-L. Variational Quantum Packaged Deflation for Arbitrary Excited States. *Quantum Eng.* **2021**, *3*, e80.

(36) McClean, J. R.; Kimchi-Schwartz, M. E.; Carter, J.; de Jong, W. A. Hybrid quantum-classical hierarchy for mitigation of decoherence and determination of excited states. *Phys. Rev. A* **2017**, *95*, 042308.

(37) Colless, J. I.; Ramasesh, V. V.; Dahlen, D.; Blok, M. S.; Kimchi-Schwartz, M.; McClean, J.; Carter, J.; De Jong, W.; Siddiqi, I. Computation of molecular spectra on a quantum processor with an error-resilient algorithm. *Phys. Rev. X* **2018**, *8*, 011021.

(38) Ollitrault, P. J.; Kandala, A.; Chen, C.-F.; Barkoutsos, P. K.; Mezzacapo, A.; Pistoia, M.; Sheldon, S.; Woerner, S.; Gambetta, J.; Tavernelli, I. Quantum equation of motion for computing molecular excitation energies on a noisy quantum processor. *arXiv(Quantum Physics)*, October 26, 2019, 1910.12890, ver. 1. <https://arxiv.org/abs/1910.12890> (accessed September 8, 2021).

(39) Motta, M.; Sun, C.; Tan, A. T.; O'Rourke, M. J.; Ye, E.; Minnich, A. J.; Brandão, F. G.; Chan, G. K.-L. Determining eigenstates and thermal states on a quantum computer using quantum imaginary time evolution. *Nat. Phys.* **2020**, *16*, 205–210.

(40) Parrish, R. M.; Hohenstein, E. G.; McMahan, P. L.; Martínez, T. J. Quantum computation of electronic transitions using a variational quantum eigensolver. *Phys. Rev. Lett.* **2019**, *122*, 230401.

(41) Parrish, R. M.; Hohenstein, E. G.; McMahan, P. L.; Martínez, T. J. Hybrid Quantum/Classical Derivative Theory: Analytical Gradients and Excited-State Dynamics for the Multistate Contracted Variational Quantum Eigensolver. *arXiv(Quantum Physics)*, June 20, 2019, 1906.08728, ver. 1. <https://arxiv.org/abs/1906.08728> (accessed September 8, 2021).

(42) Nakanishi, K. M.; Mitarai, K.; Fujii, K. Subspace-search variational quantum eigensolver for excited states. *Phys. Rev. Res.* **2019**, *1*, 033062.

(43) Zhang, D.-B.; Yuan, Z.-H.; Yin, T. Variational quantum eigensolvers by variance minimization. *arXiv(Quantum Physics)* June 29, 2020, 2006.15781, ver. 1. <https://arxiv.org/abs/2006.15781> (accessed September 8, 2021).

(44) Parrish, R. M.; McMahan, P. L. Quantum filter diagonalization: Quantum eigendecomposition without full quantum phase estimation. *arXiv(Quantum Physics)* September 19, 2019, 1909.08925, ver. 1. <https://arxiv.org/abs/1909.08925> (accessed September 8, 2021).

(45) Bespalova, T. A.; Kyriienko, O. Hamiltonian operator approximation for energy measurement and ground state preparation. *arXiv(Quantum Physics)*, September 7, 2020, 2009.03351, ver. 1. <https://arxiv.org/abs/2009.03351v1> (accessed September 8, 2021).

(46) Jensen, F. *Introduction to computational chemistry*; John Wiley & Sons, 2017.

(47) Mitarai, K.; Nakagawa, Y. O.; Mizukami, W. Theory of analytical energy derivatives for the variational quantum eigensolver. *Phys. Rev. Res.* **2020**, *2*, 013129.

(48) O'Brien, T. E.; Senjean, B.; Sagastizabal, R.; Bonet-Monroig, X.; Dutkiewicz, A.; Buda, F.; DiCarlo, L.; Visscher, L. Calculating energy derivatives for quantum chemistry on a quantum computer. *npj Quantum Inf.* **2019**, *5*, 1–12.

(49) Azad, U.; Singh, H. Quantum Chemistry Calculations using Energy Derivatives on Quantum Computers. *arXiv(Quantum Physics)* June 10, 2021, 2106.06463, ver. 1. <https://arxiv.org/abs/2106.06463> (accessed September 8, 2021).

(50) Sokolov, I. O.; Barkoutsos, P. K.; Moeller, L.; Suchsland, P.; Mazzola, G.; Tavernelli, I. Microcanonical and finite-temperature ab initio molecular dynamics simulations on quantum computers. *Phys. Rev. Research* **2021**, *3*, 013125.

(51) Mizukami, W.; Mitarai, K.; Nakagawa, Y. O.; Yamamoto, T.; Yan, T.; Ohnishi, Y.-y. Orbital optimized unitary coupled cluster theory for quantum computer. *arXiv(Condensed Matter, Strongly Correlated Electrons)*, October 25, 2019, 1910.11526, ver. 1. <https://arxiv.org/abs/1910.11526v1> (accessed September 8, 2021).

(52) Helgaker, T. U.; Almlöf, J. A second-quantization approach to the analytical evaluation of response properties for perturbation-dependent basis sets. *Int. J. Quantum Chem.* **1984**, *26*, 275–291.

(53) Mitarai, K.; Negoro, M.; Kitagawa, M.; Fujii, K. Quantum circuit learning. *Phys. Rev. A* **2018**, *98*, 032309.

- (54) Evangelista, F. A.; Chan, G. K.-L.; Scuseria, G. E. Exact parameterization of fermionic wave functions via unitary coupled cluster theory. *J. Chem. Phys.* **2019**, *151*, 244112.
- (55) Tamiya, S.; Koh, S.; Nakagawa, Y. O. Calculating nonadiabatic couplings and Berry's phase by variational quantum eigensolvers. *Phys. Rev. Research* **2021**, *3*, 023244.
- (56) Chahre, M. Trigger and amplification mechanisms in visual phototransduction. *Annu. rev. biophys. biophys. chem.* **1985**, *14*, 331–360.
- (57) Birge, R. R. Nature of the primary photochemical events in rhodopsin and bacteriorhodopsin. *Biochim. Biophys. Acta - Bioenerg.* **1990**, *1016*, 293–327.
- (58) Schnedermann, C.; Yang, X.; Liebel, M.; Spillane, K.; Lugtenburg, J.; Fernández, I.; Valentini, A.; Schapiro, I.; Olivucci, M.; Kukura, P.; et al. Evidence for a vibrational phase-dependent isotope effect on the photochemistry of vision. *Nature Chem.* **2018**, *10*, 449–455.
- (59) Fdez. Galvan, I.; Vacher, M.; Alavi, A.; Angeli, C.; Aquilante, F.; Autschbach, J.; Bao, J. J.; Bokarev, S. I.; Bogdanov, N. A.; Carlson, R. K.; Chibotaru, L. F.; Creutzberg, J.; Dattani, N.; Delcey, M. G.; Dong, S. S.; Dreuw, A.; Freitag, L.; Frutos, L. M.; Gagliardi, L.; Gendron, F.; Giussani, A.; Gonzalez, L.; Grell, G.; Guo, M.; Hoyer, C. E.; Johansson, M.; Keller, S.; Knecht, S.; Kovacevic, G.; Kallman, E.; Li Manni, G.; Lundberg, M.; Ma, Y.; Mai, S.; Malhado, J. P.; Malmqvist, P. A.; Marquetand, P.; Mewes, S. A.; Norell, J.; Olivucci, M.; Oppel, M.; Phung, Q. M.; Pierloot, K.; Plasser, F.; Reiher, M.; Sand, A. M.; Schapiro, I.; Sharma, P.; Stein, C. J.; Sørensen, L. K.; Truhlar, D. G.; Ugandi, M.; Ungur, L.; Valentini, A.; Vancollie, S.; Veryazov, V.; Weser, O.; Wesolowski, T. A.; Widmark, P.-O.; Wouters, S.; Zech, A.; Zobel, J. P.; Lindh, R. OpenMolcas: From Source Code to Insight. *J. Chem. Theory Comput.* **2019**, *15*, 5925–5964. PMID: 31509407.
- (60) Smith, D. G.; Burns, L. A.; Simonnet, A. C.; Parrish, R. M.; Schieber, M. C.; Galvelis, R.; Kraus, P.; Kruse, H.; Di Remigio, R.; Alenaizan, A.; et al. PSI4 1.4: Open-source software for high-throughput quantum chemistry. *J. Chem. Phys.* **2020**, *152*, 184108.
- (61) McClean, J. R.; Rubin, N. C.; Sung, K. J.; Kivlichan, I. D.; Bonet-Monroig, X.; Cao, Y.; Dai, C.; Fried, E. S.; Gidney, C.; Gimby, B.; Gokhale, P.; Häner, T.; Hardikar, T.; Havlíček, V.; Higgott, O.; Huang, C.; Izaac, J.; Jiang, J.; Liu, X.; McArdle, S.; Neeley, M.; O'Brien, T.; O'Gorman, B.; Ozfidan, I.; Radin, M. D.; Romero, J.; Sawaya, N. P. D.; Senjean, B.; Setia, K.; Sim, S.; Steiger, D. S.; Steudtner, M.; Sun, Q.; Sun, W.; Wang, D.; Zhang, F.; Babbush, R. OpenFermion: the electronic structure package for quantum computers. *Quantum Sci. Technol.* **2020**, *5*, 034014.
- (62) Cirq Developers. 2021; DOI: 10.5281/zenodo.5182845, See full list of authors on Github: <https://github.com/quantumlib/Cirq/graphs/contributors> (accessed September 8, 2021).
- (63) Yarkony, D. R. Systematic determination of intersections of potential energy surfaces using a Lagrange multiplier constrained procedure. *J. Phys. Chem.* **1993**, *97*, 4407–4412.
- (64) Yarkony, D. R. Theoretical studies of spin-forbidden radiationless decay in polyatomic systems: insights from recently developed computational methods. *J. Am. Chem. Soc.* **1992**, *114*, 5406–5411.
- (65) Bearpark, M. J.; Robb, M. A.; Schlegel, H. B. A direct method for the location of the lowest energy point on a potential surface crossing. *Chem. Phys. Lett.* **1994**, *223*, 269–274.
- (66) Keal, T. W.; Koslowski, A.; Thiel, W. Comparison of algorithms for conical intersection optimization using semiempirical methods. *Theor. Chem. Acc.* **2007**, *118*, 837–844.
- (67) Sicilia, F.; Blancafort, L.; Bearpark, M. J.; Robb, M. A. New Algorithms for Optimizing and Linking Conical Intersection Points. *J. Chem. Theory Comput.* **2008**, *4*, 257–266. PMID: 26620657.
- (68) Cederbaum, L.; Schirmer, J.; Meyer, H.-D. Block diagonalisation of Hermitian matrices. *J. Phys. A Math. Theor.* **1989**, *22*, 2427.
- (69) Richter, M.; Marquetand, P.; González-Vázquez, J.; Sola, I.; González, L. SHARC: ab initio Molecular Dynamics with Surface Hopping in the Adiabatic Representation Including Arbitrary Couplings. *J. Chem. Theory Comput.* **2011**, *7*, 1253–1258.
- (70) Tully, J. C. Molecular dynamics with electronic transitions. *J. Chem. Phys.* **1998**, *93*, 1061–1071.
- (71) Andrade, X.; Castro, A.; Zueco, D.; Alonso, J. L.; Echenique, P.; Falcieto, F.; Rubio, A. Modified Ehrenfest Formalism for Efficient Large-Scale ab initio Molecular Dynamics. *J. Chem. Theory Comput.* **2009**, *5*, 728–742.
- (72) Arimitsu, K.; Nakagawa, Y. O.; Koh, S.; Mizukami, W.; Gao, Q.; Kobayashi, T. Analytic energy gradient for state-averaged orbital-optimized variational quantum eigensolvers and its application to a photochemical reaction. *arXiv(Physics, Chemical Physics)*, July 27, 2021, 2107.12705, ver. 1. <https://arxiv.org/abs/2107.12705> (accessed September 8, 2021).
- (73) Li, Y.; Benjamin, S. C. Efficient variational quantum simulator incorporating active error minimization. *Phys. Rev. X* **2017**, *7*, 021050.
- (74) Schuld, M.; Bergholm, V.; Gogolin, C.; Izaac, J.; Killoran, N. Evaluating analytic gradients on quantum hardware. *Phys. Rev. A* **2019**, *99*, 032331.
- (75) Mari, A.; Bromley, T. R.; Killoran, N. Estimating the gradient and higher-order derivatives on quantum hardware. *arXiv(Quantum Physics)* Aug 14, 2020, 2008.06517, ver. 1. <https://arxiv.org/abs/2008.06517v1> (accessed September 8, 2021).
- (76) Meyer, J. J. Gradients just got more flexible. *Quantum Views* **2021**, *5*, 50.
- (77) Hubregtsen, T.; Wilde, F.; Qasim, S.; Eisert, J. Single-component gradient rules for variational quantum algorithms. *arXiv(Quantum Physics)*, June 2, 2021, 2106.01388, ver. 1. <https://arxiv.org/abs/2106.01388> (accessed September 8, 2021).
- (78) Romero, J.; Babbush, R.; McClean, J. R.; Hempel, C.; Love, P. J.; Aspuru-Guzik, A. Strategies for quantum computing molecular energies using the unitary coupled cluster ansatz. *Quantum Sci. Technol.* **2019**, *4*, 014008.
- (79) Kottmann, J. S.; Anand, A.; Aspuru-Guzik, A. A Feasible Approach for Automatically Differentiable Unitary Coupled-Cluster on Quantum Computers. *arXiv(Quantum Physics)*, November 11, 2020, 2011.05938, ver. 1. <https://arxiv.org/abs/2011.05938> (accessed September 8, 2021).
- (80) Crooks, G. E. Gradients of parameterized quantum gates using the parameter-shift rule and gate decomposition. *arXiv(Quantum Physics)*, May 30, 2019, 1905.13311, ver. 1. <https://arxiv.org/abs/1905.13311> (accessed September 8, 2021).
- (81) Banchi, L.; Crooks, G. E. Measuring Analytic Gradients of General Quantum Evolution with the Stochastic Parameter Shift Rule. *arXiv(Quantum Physics)* May 20, 2020, 2005.10299, ver. 2. <https://arxiv.org/abs/2005.10299> (accessed September 8, 2021).
- (82) Wierichs, D.; Izaac, J.; Wang, C.; Lin, C. Y.-Y. General parameter-shift rules for quantum gradients. *arXiv(Quantum Physics)*, September 30, 2021, 2107.12390, ver. 2. <https://arxiv.org/abs/2107.12390> (accessed September 8, 2021).
- (83) Izmaylov, A. F.; Lang, R. A.; Yen, T.-C. Analytic gradients in variational quantum algorithms: Algebraic extensions of the parameter-shift rule to general unitary transformations. *arXiv(Quantum Physics)* December 19, 2021, 2107.08131, ver. 4. <https://arxiv.org/abs/2107.08131> (accessed September 8, 2021).
- (84) Helgaker, T.; Jørgensen, P. Analytical calculation of geometrical derivatives in molecular electronic structure theory. *Adv. Quantum Chem.* **1988**, *19*, 183–245.
- (85) Simons, J.; Jørgensen, P.; Helgaker, T. U. Higher molecular-deformation derivatives of the configuration-interaction energy. *Chem. Phys.* **1984**, *86*, 413–432.